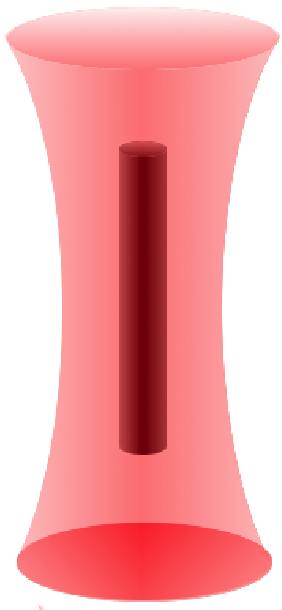

A study of periodic and quasi-periodic orientational motion of microrods in a shear flow using optical tweezers

M.Sc. Thesis in Complex Adaptive Systems

Alexander Laas

Department of Physics & Engineering Physics
Non-linear Dynamics & Statistical Physics
Chalmers University of Technology
Gothenburg, Sweden 2014
M.Sc. Thesis 2014

Abstract

The orientational motions of single isolated inertialess microrods are studied in a reversible creeping shear flow. In previous work [12, 24, 30] it was observed that rodlike particles could experience both periodic and quasi-periodic behavior. This work studies how the orientational motion, including periodic and quasi-periodic motion, depends upon the orientational initial conditions, for a single microrod. For the purpose of changing the initial conditions, optical tweezers are installed in the experimental setup. In order to demonstrate that the microdrods and fluid are inertialess the flow is reversed and the trajectories before and after the reversal are analyzed. If both the microrod and the flow are inertialess, the orientational motion of the rod is expected to retrace itself when the flow is reversed. The experimental results show that if the flow is reversed smoothly, particles can show this retraceibility. The experimental results also demonstrate that a single rod may exhibit either periodic or quasi-periodic motion, depending solely on its orientational initial condition. The observable dynamics show good agreement with Jeffery's equations of motion for an inertialess ellipsoid in a creeping shear flow.

Acknowledgements

The work for this thesis has been made under the supervision of Professors Bernhard Mehlig and Dag Hanstorp.

Thank you, Bernhard, your enthusiasm have been encouraging to continue to strive to make the results better. A big thank you to Dag, you have been a great support when working on the experimental setup and throughout the whole process. Also a special thanks to Jonas Einarsson, Besira Mihiretie and the staff at the 8th floor of Forskarhuset, I have been bugging most of you with different requests and you have all been very helpful. And of course a thanks to Staffan Ankardal, it was a pleasant experience doing the experiments together.

Alexander Laas, Gothenburg 20/5/14

Contents

The experiments were conducted in collaboration with Staffan Ankardal, a fellow M.Sc. student [2].

1

Introduction

The subject of this thesis, transportation of small particles suspended in a microchannel shear flow, is part of the general field of fluid mechanics. Understanding particle transportation is relevant in a variety of applications. For instance, the growth of ice crystals in clouds [9], or the motion of microorganisms, such as plankton in viscous flows [17]. Particle transportation in flows also has a range of industrial and biomedical applications [6, 13, 18, 33, 34].

Jeffery [23] derived equations of motion for inertialess ellipsoids in a linear creeping shear flow. For axisymmetric ellipsoids he solved the equations and showed that the solutions are periodic. Bretherton [7] later on showed that Jeffery's equations are valid for any axisymmetric particle. Jeffery's equations have been used to interpret experimental results and make theoretical predictions in a number of research studies [1, 11, 16, 22, 26, 28, 38]. However, most experimental research of particle motion in flows has involved axisymmetric particles and only a few experimental studies cover the case of non-axisymmetric particles.

Both Hinch and Leal [21] and Yarin *et al.* [41] analysed Jeffery's equations analytically and numerically for the case of non-axisymmetric ellipsoids. The main outcome of their work describes how the orientational motion of non-axisymmetric ellipsoids differs from that of axisymmetric ones. Hinch and Leal found that the non-axisymmetric ellipsoids have orientational motions that are doubly periodic. Yarin *et al.* further showed that a non-axisymmetric ellipsoid might experience either periodic or doubly periodic motion, depending solely on its initial orientation. For some ellipsoids they also found that the motion could be chaotic. Yarin *et al.* refer to the doubly periodic motion as quasi-periodic motion.

1.1 Motivation

In nature, most particles are irregular in shape and therefore their orientational motion cannot be described by simple equations. This is why experimental studies of the orientational dynamics of such particles are of paramount importance.

The work of Einarsson *et al.* [12], the precursor of this study, found empirical evidence for both periodic and quasi-periodic motion of rod-like particles by observing the motion of polymer microparticles in a microchannel shear flow. The degree of asymmetry of the particles, however, could not be quantified due to the limited resolution of the microscope. Another limitation Einarsson *et al.* faced was that different types of motion could only be observed using different particles. The question arose as to whether or not it might be possible to unequivocally demonstrate the dependence of initial orientation of the rods for periodic and quasi-periodic motion. The motivation of this thesis is to find an answer to this question.

1.2 Method and disposition of this thesis

The orientational motions of the particles are observed in a shear flow through a rectangular microfluidic channel, in the same way as in the work of Einarsson *et al.* [12]. But the particles used here are different from those used in [12]. Micron-sized glass rods replace the irregularly shaped polymer particles. Each microrod has a very precisely defined diameter of 3μm. But, the level of asymmetry varies as a result of irregularities at their ends. The rods are manufactured by the Japanese company Nippon Electric Glass Co., Ltd and the irregularities are likely a consequence of the fabrication method of the rods. The rods are manufactured by cutting monofilament glass [8] and the cutting is thought to cause the deformed ends. To change the initial orientation of the rods, optical tweezers are installed in the present apparatus.

The thesis is divided into two parts. In the first part, theory of optical forces and the installation of optical tweezers are described. The purpose of the tweezers is to change the initial conditions of a particle and to position it at a suitable location in the microchannel. The second part of the thesis includes a brief introduction to the relevant fluid dynamics and Jeffery's equations of motion for an ellipsoidal particle. Further, it covers the experimental data collection and analysis.

Part I

Optical tweezers

2

Theory

THE principle of optical manipulation is based on the fact that light carries momentum. Newton's second law of motion state that the momentum for an isolated system is conserved. And whenever a photon is absorbed, reflected or refracted by an object, its momentum changes. Hence, the change in momentum experienced by the photon is imparted to the object it interacts with. From Newton's laws of motion, this means that both the object and photon exert forces upon each other. The force exerted by the photon upon the object is called an optical force. For macroscopic objects optical forces can be neglected. However, using a high-intensity light source such as a laser, it is possible to achieve a resulting force sufficiently powerful to manipulate microscopic objects.

This chapter aims at explaining the theory behind optical tweezers. It also explains how it is possible to use optical tweezers to move and rotate cylindrical particles.

Most available theory of optical manipulation describes applications to spheres but the principles can easily be applied to cylinders. As opposed to the case of spheres there are no exact analytical solutions for the optical forces that work on a cylindrical particle in optical tweezers. However, there are both experimental and numerical studies of the subject [4, 5]. The second part of this chapter presents the results of the numerical study by Gauthier [14] that describes the behavior of cylindrical rods in optical tweezers.

2.1 Optical forces

The momentum p for a photon is given by

$$p = \frac{h}{\lambda}, \tag{2.1}$$

where h is Planck's constant and λ is the wavelength of the photon. The direction of the momentum points in the direction of propagation, i.e. the direction of the wave vector $\mathbf{k}$, ($|\mathbf{k}| = 2\pi/\lambda$). When photons are absorbed, refracted and reflected their linear momentum is changed according to

$$\Delta\mathbf{p} = \hbar(\mathbf{k}' - \mathbf{k}), \tag{2.2}$$

where $\mathbf{k}$ and $\mathbf{k}'$ are the wave vectors for a single photon before and after the interaction and $\hbar$ is the reduced Planks constant.

The functionality of optical tweezers in this section is explained using ray optics. However, ray optics is only applicable when the illuminated object is much larger than the wavelength of the light [37]. For particles much smaller than the wavelength, the ray-optics approximation cannot be used. Such particles are said to belong to the Rayleigh-regime [19], where electromagnetic theory is used to describe how the optical forces arise. Due to the large dimensions of the microrods used in the experiments compared to the wavelength of the laser, the microrods are not in the Rayleigh-regime and the details for optical forces for particles in that regime are therefore not discussed further in this thesis. The details of optical forces for particles in the Rayleigh-regime can be found in [19].

Using ray optics, light rays are considered to move as straight lines. The rays obey the laws of reflection and refraction at boundaries between two medias of different refractive index [20]. To describe the principles of optical tweezers a spherical particle is used as an example.

Consider a transparent spherical bead placed in a collimated laser beam with Gaussian intensity distribution, shown in Figure 2.1. The bead acts as a lens and refracts the incoming rays, thus changing their direction and hence their $\mathbf{k}$-vector. If the spherical bead is positioned off-axis from the center of the beam, the intensity distribution over the bead is unbalanced. One of the sides is exposed to higher intensity and more momentum is therefore transferred on that side. Assuming that the index of refraction of the sphere is greater than that of the medium, this results in a net force $\mathbf{F}_{tot}$ on the particle where the component in the plane perpendicular to the beam direction point towards the center of the beam as shown in Figure 2.1. A collimated Gaussian beam, however, only provides a trap in the plane perpendicular to the beam axis, i.e. a two-dimensional trap.

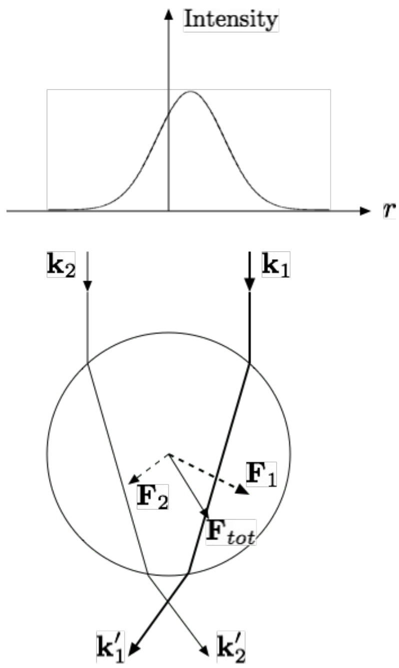

Figure 2.1: Collimated rays incident on a spherical bead. The bead is positioned off-axis from the center of the beam which gives rise to an unbalanced intensity distribution. The light rays are incident in the directions of $\mathbf{k_1}$ and $\mathbf{k_2}$, where the two vectors represent the sums of all wave vectors that are incident on the right and left side of the center of the bead, respectively. The rays leave the bead in the directions of $\mathbf{k'_1}$ and $\mathbf{k'_2}$. The intensity is higher in ray $\mathbf{k_1}$ and hence the change in momentum from $\mathbf{k}_1$ to $\mathbf{k}'_1$ is greater than from $\mathbf{k}_2$ to $\mathbf{k}'_2$. This gives rise to an optical force that pushes the bead towards the center of the beam.

In order to trap a particle in three dimensions the incident rays need to be focused. Three-dimensional trapping of a spherical particle can be explained by decomposing the total optical force $\mathbf{F}_{tot}$ into two orthogonal components; the scattering force $\mathbf{F}_s$ and the gradient force $\mathbf{F}_g$. The scattering force points in the direction of propagation of the incident ray, while the gradient force points perpendicular towards the extended path of the incident ray (see Figure 2.2). By neglecting absorption, Ashkin [3] derived the following expressions for the gradient and scattering force, exerted by a single ray on a sphere:

$$F_s = \frac{n_1 P}{c}\left\{1 + R\,\cos 2\theta_i - \frac{T^2[\cos(2\theta_i - 2\theta_t) + R\,\cos 2\theta_i]}{1 + R^2 + 2R\,\cos 2\theta_t}\right\} \tag{2.3a}$$

and (2.3b)

$$F_g = \frac{n_1 P}{c}\left\{R\,\sin 2\theta_i - \frac{T^2[\cos(2\theta_i - 2\theta_t) + R\,\sin 2\theta_i]}{1 + R^2 + 2R\,\cos 2\theta_t}\right\}. \tag{2.3c}$$

Here R and T are the reflection and transmission coefficients, given by Fresnel's relations, which specify the proportion of the beam power P that is reflected and transmitted, respectively. θ_i and θ_t are the incidence and transmittance angles, n_1 is the refractive index of the surrounding medium, n_2 is the refractive index of the spherical bead and c is the speed of light in vacuum, see Figure 2.2.

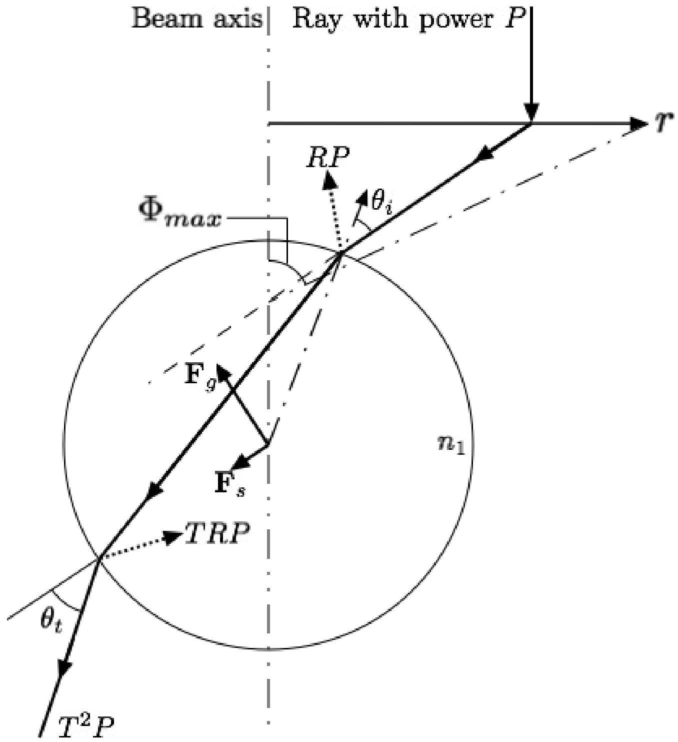

Figure 2.2: The contribution from a single incoming ray is a calculated from Eqs. (2.3). When a ray reaches the boundary between the sphere and the surrounding media it is either reflected or transmitted. The proportion of light that is transmitted or reflected is decided by the transmission and reflection coefficients T and R, calculated from Fresnel's relations. In order to calculate the optical force for a single ray, the contributions from all internal reflections R^nT^2P need to be taken into account, which is done in Eqs. (2.3). (This discussion assumes that absorption is neglected). Φ_{max} denotes the maximum angle of convergence.

The total net force acting on a spherical bead is obtained by summing up the contributions from all incident rays,

$$\mathbf{F}_{tot} = \sum_{\text{rays}} \mathbf{F}_g + \sum_{\text{rays}} \mathbf{F}_s, \tag{2.4}$$

where the forces $\mathbf{F}_g$ and $\mathbf{F}_s$ are calculated from Eqs. (2.3). In order to trap a particle in all three dimensions, the contributions to the gradient force must exceed the contributions to the scattering force along the beam axis. This is achieved in optical tweezers by a highly focused laser beam, as shown in Figure 2.3. The sharp convergence of the beam causes a high proportion of the scattering force to act in the plane perpendicular to the beam axis. The contributions from different rays to the total scattering force that acts perpendicular to the beam axis, cancel each other out. The contribution to the total scattering force that acts along the beam axis for a focused beam is small, which allows the gradient force to be dominant. When the gradient force is dominant along the the beam axis the resulting force $\mathbf{F}_{tot}$ points towards the focus of the incoming beam [3].

From Eqs. (2.3), it is not obvious how the relative refractive index n_2/n_1 between the surrounding media and the illuminated sphere affects the forces $\mathbf{F}_s$ and $\mathbf{F}_g$. A high relative refractive index gives a higher angle of refraction but it also means that a higher proportion of the light is reflected. This in turn gives a higher contribution to the scattering force. For a sphere, Ashkin [3] found the optimal relative refractive index to be 1.2.

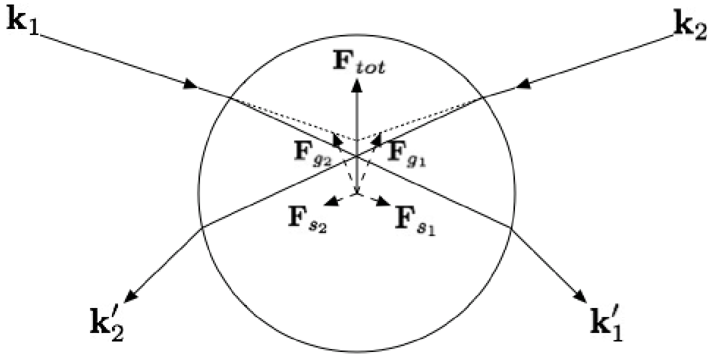

Figure 2.3: In order to trap a particle in more than two dimensions the gradient force $\mathbf{F}_g$ needs to exceed the scattering force $\mathbf{F}_s$ along the beam axis. The resulting force then points towards the focus of the incident rays, (the dotted lines).

2.1.1 Trapping cylindrical particles

The principles of optical forces described in the previous section also apply to cylindrical particles. However, theoretical analysis of the total force $\mathbf{F}_{tot}$ is more complicated and numerical analysis is therefore preferred.

In this section a summary of the numerical results obtained by Gauthier [14] is presented in order to give an understanding of the experimental results presented later in this thesis. Gauthier's calculations are based on the ray optics approach, and where needed, EM-theory was used [14].

The numerical calculations are based on the lowest Gaussian intensity profile, where the intensity has a single peak located in the center of the beam, the same intensity distribution as the laser used in the experiments for this thesis.

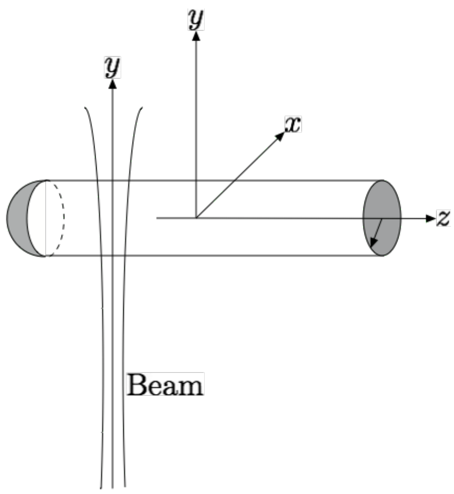

Figure 2.4: The figure shows a cylinder with one spherical and one flat end. Gauthier [14] calculated the forces exerted from optical tweezers for cylinders with both types end faces.

An optical trap is defined as an optical force field in which a particle is in spatial equilibrium. Compared to the case of spherical particles the geometry of a cylinder makes it necessary to also consider the torque $\boldsymbol{\tau}$ in order to find the rotational equilibrium.

Figure 2.4 shows the coordinate system that Gauthier used. The interaction between the rod and the beam is independent of how the rod is rotated in the x-z-plane. For simplicity the following discussion assumes the rod to be in the y-z-plane.

When a rod is positioned as in Figure 2.4, Gauthier concluded that the force components F_x and F_z are both zero. For the x-direction, any small displacement induces a restoring force F_x, due to intensity gradient, which brings the rod back to the center of the beam. This is the same reasoning as for the spherical particles, as described in the previous section. A restoring force F_z is only induced if the beam interacts with one of the rod ends.

As long as the rod is aligned with the z-axis the torque vanishes, but this is not a stable position. Any displacement of the rod by an angle θ in the y-z-plane gives rise to a torque τ_x around the x-axis. The torque works to increase the displacement θ, as shown in Figure 2.5. As the displacement θ increases, the torque increase and it rotates the rod until it is aligned with the y-axis.

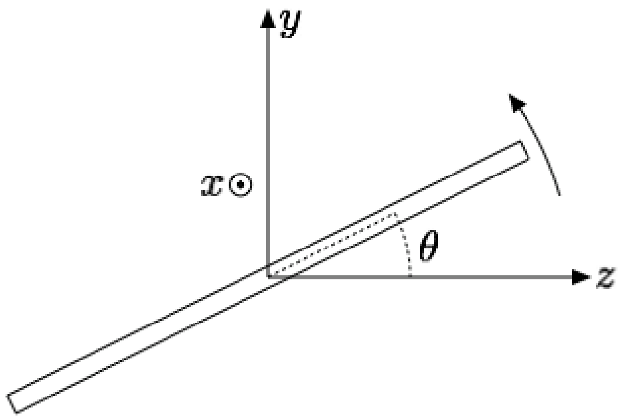

Figure 2.5: A displacement θ in the y-z-plane for a rod aligned with the z-axis gives rise to a torque τ_x around the x-axis. According to Gauthier [14], the torque works to increase the displacement until the rod is aligned with the y-axis.

The only stable orientation of the rod where the torque is at equilibrium is when it is aligned with the direction of the beam, i.e. along the y-axis.

When a cylinder is aligned with the y-axis, only the radial force F_r and the force along the y-axis F_y need to be considered. According to Gauthier [14], the force F_y on the rod is capable only of canceling the gravitational force. F_y in this case arises due to radiation pressure from the beam. Matching the density between the fluid and particles eliminates the gravitational force component for the particles in the experiments for this thesis. Gauthier does not provide any information about the possibilities of trapping a cylindrical particle along the beam direction in the absence of a gravitational component. However, Gauthier concludes the force F_r to be stable when a rod is aligned with the y-axis.

The numerical results by Gauthier are also consistent with experimental observations made by Sun *et al.* [36] and Neves *et al.* [31].

3

Optical setup

THERE are two fundamental components needed when setting up optical tweezers. Firstly, a powerful light source such as a laser is needed and secondly, a lens is required to focus the light beam onto the sample. However, with only these two components it is difficult to get high-precision optical tweezers. In this chapter the optical setup for the optical tweezers is described. It is also further described how the optical tweezers are used to change the orientational initial conditions and the center of mass position of a particle in the experiments.

3.1 Installing optical tweezers

The laser that is used for the optical tweezers has a wavelength in the infrared spectrum (1060-1064nm). The light from the laser is focused with a microscope objective, the same objective that is also used to observe the particles. For a microscope objective the maximum angle of convergence is determined by the numerical aperture (N.A.), defined by

$$N.A. = n_1 \, \sin \Phi_{max}, \tag{3.1}$$

where n_1 is the refractive index of the working medium, see Figure 3.1. The quality of the optical trap created by the tweezers is highly dependent on the maximum angle of convergence Φ_{max}, since it determines the maximum convergence of the incoming beam.

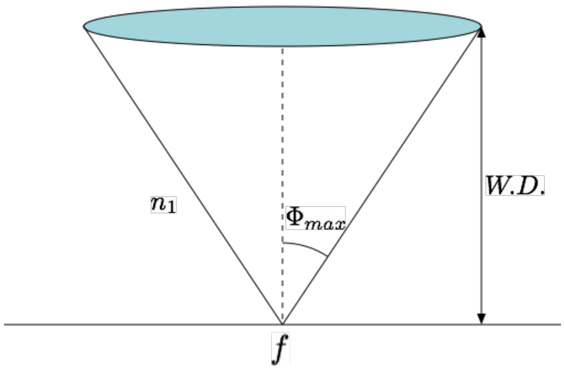

Figure 3.1: The figure shows the definition of the maximum angle of convergence Φ_{max} and the working distance W.D. The working distance describes the distance from the front end of the lens to the closest part of the sample in focus. The numerical aperture (N.A.) is calculated with respect to the focal point f and it is a function of Φ_{max} and the index of refraction of the working medium.

The objective used to trap the particles has a numerical aperture (N.A.) of 1.0 and a working distance (W.D.) of 2mm. The working distance is also shown in Figure 3.1 and it specifies the distance from the front end of the lens to the image plane. With a high W.D. it is possible to trap particles deeper into a sample.

In Figure 3.2 a drawing of the optical setup is shown. The figure shows how the laser is directed into the microscope entry and onto the sample through the microscope objective.

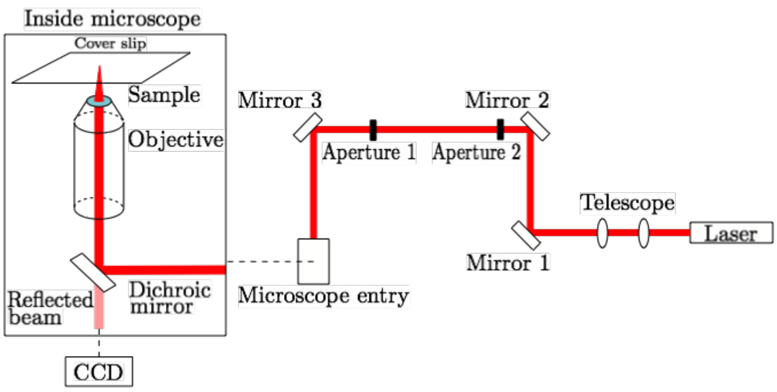

Figure 3.2: A schematic of the optical setup. The laser is directed into the microscope entry using mirrors 1 and 2. Each mirror controls two degrees of freedom and they are adjusted so that the laser passes through the center of the objective lens. The telescope is used to magnify the beam radius to make sure the laser overfill the objective entrance aperture. A small fraction of the laser light is reflected on the cover slip, and eventually reaches the CCD. The laser light that enters the CCD is however small, since the dichroic mirror reflects the IR-light of the laser.

3.2 Working medium

The microscope objective used in this work is designed for water immersion. However, it is not possible to use pure water as the working medium since the density of the medium needs to be matched to that of the particles. The fluid used is instead a mixture of water, glycerol and *sodium metatungstate monohydrate* (SMTS). The last ingredient is a wolfram-based substance with a high density and it is mixed with the other two liquids in order to increase the density of the fluid.

As seen in Eq. (3.1) the maximum angle of convergence is affected by the refractive index of the working medium. Water and glycerol have refractive indices of 1.33 and 1.46, respectively. SMTS has a refractive index of 1.56, which is the same as the refractive index of the glass particles. The volume of the mixture consists of 9% glycerol, 16.5% water and 74.5% SMTS. To calculate the refractive index of the mixture, the *Lorentz-Lorenz* formula [29] is used,

$$\frac{n_{tot}^2 - 1}{n_{tot}^2 + 2} = \sum_{\text{ingredients}} w_{\mathrm{i}} \frac{n_i^2 - 1}{n_i^2 + 2}, \tag{3.2}$$

where w_i denotes the volume fraction for each ingredient in the mixture, n_i is the respective index of refraction. Eq. (3.2) gives the mixture a refractive index of 1.51 and the corresponding maximum angle of convergence is calculated to be 41.47° from Eq. (3.1).

3.3 Manipulation of particles

The microchannel is mounted on a moveable stage that is used to change the relative position between the channel and the microscope objective. It turns out to be easier to move the microchannel than the microscope objective. Thus, instead of moving a particle the channel is moved and the particle is kept in place by the laser.

The optical tweezers were tested by trapping spherical particles and an example is shown in Figure 3.3.

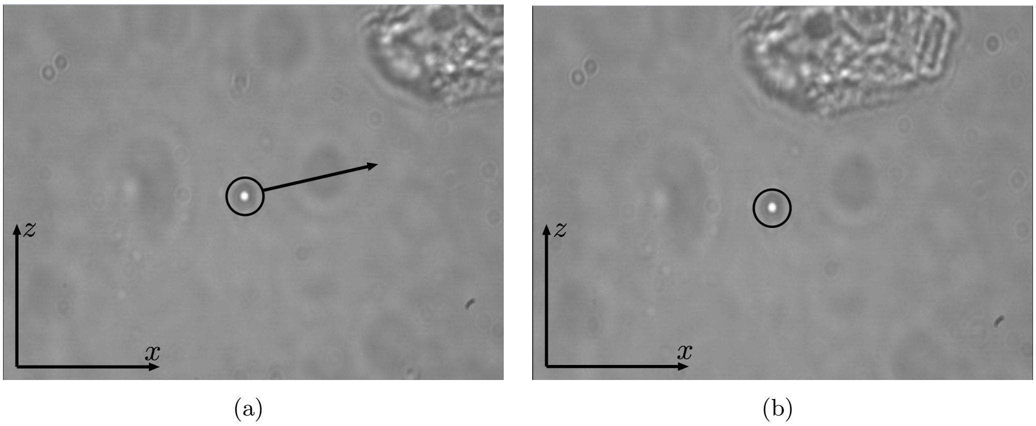

Figure 3.3: The spherical bead is trapped by the optical tweezers and moved around in the channel. By moving the channel, the bead is "relocated" since it is held fixed by the tweezers. This is why the bead is kept centered in the two figures whereas the background moves.

As explained in Section 2.1.1, a cylindrical rod is in its equilibrium position when it is aligned with the beam axis and the experiments show that the optical tweezers quickly aligns a rod. An example of this is shown in Figure 3.4.

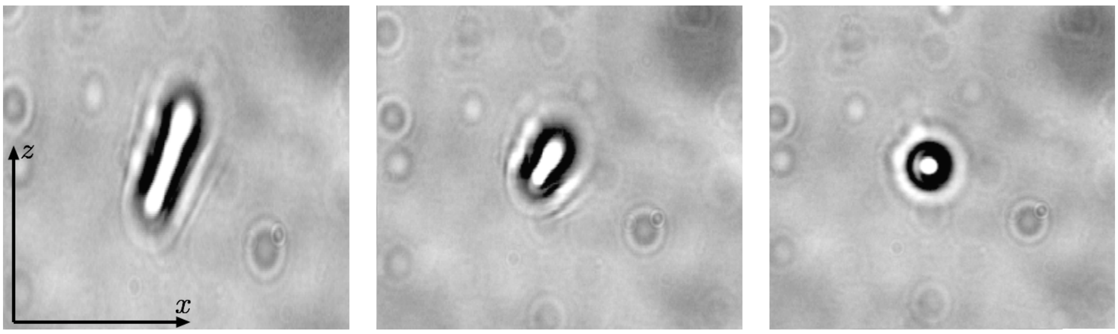

Figure 3.4: The figure shows the process of trapping a rod. The sequence from left to right, illustrates how the rod aligns with the direction of the laser, i.e. the beam axis, where it is in stable spatial equilibrium.

The optical tweezers are found to trap a particle in all three spatial dimensions and it is hence possible to position it anywhere in the channel. By changing the focus of the objective a rod can be moved along the beam direction. This is a result that was not predicted in the work of Gauthier [14], as discussed in Section 2.1.1.

By moving the channel it is possible to change both the position and orientation of a particle. The repositioning and reorientation of a particle is illustrated and described in Figure 3.5.

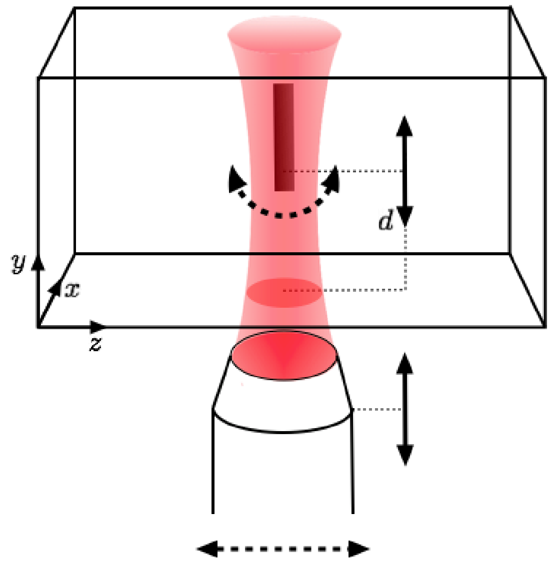

Figure 3.5: A rod can be trapped with an optical power of 0.35-0.45W. By moving the channel with different speeds in the x-z-plane, a rod can be either rotated or repositioned. In the experiments it was observed that a rod is trapped in the end that is closest to the objective. When moving the sample, the trapped end is held fixed by the tweezers while the rest of the rod aligns with the direction of change. In this way it is possible to rotate a rod. To change its position, the channel needs to be moved slowly. By doing this, the rotation caused by the movement is counteracted by the torque from the tweezers. The particle stays aligned and trapped as the channel is moved. A particle can be moved in the y-direction by changing the focus of the objective. d denotes the distance from the channel floor to the trapped end of a particle.

In the experiments it was observed that a rod is trapped in the end that is closest to the objective. Thus, when the channel is moved an additional torque τ_f is induced on the rod around the point where the rod is trapped, by the fluid. If the channel is moved slowly the induced torque τ_f is less than the torque from the optical tweezers. The rod then stays aligned with the y-axis as the channel is moved and the particle is repositioned. To change the orientation of a rod, the channel is moved faster, so that the induced torque τ_f exceeds the torque from the tweezers. The rod then aligns with the direction of movement. With this procedure it is possible to alternate the orientation of the rod between the beam axis and the direction of the movement.

Ingber and Mondy [22] did a numerical study of the orientational motion of ellipsoids and rods in a shear flow in proximity of a wall. They found that the orientational trajectory of the particles is unaffected as close as one particle length from the walls. The distance from the trapped end of a particle to the bottom of the channel is known since it is the same as the distance from the focus to the bottom, denoted d in Figure 3.5. The typical rod length L_{rod} of the particles used in the experiments is approximately 20μm. Knowing d and L_{rod} makes it is possible to position a rod on a distance from channel walls such that it can be assured that the motion is unaffected.

Part II

Particle dynamics

4

Theory

THE objective of this thesis is to study the orientational motion of particles under the same conditions that were assumed by Jeffery [23]. Jeffery derived equations of motion for an arbitrary ellipsoid immersed in a linear creeping shear flow. In order to understand what these conditions mean, a brief summary of fluid dynamics is needed. The Navier-Stokes equation is introduced, from where the Reynolds number for a flow is derived. The Reynolds number is a dimensionless number used to characterize the flow. This thesis focuses on low Reynolds number fluidics and the difference between a high and low Reynolds number is discussed. At the end of this chapter, Jeffery's equations are presented together with numerical and analytical results that describe the dynamics investigated.

4.1 Fluid dynamics

The character of a flow can be divided into three main types; laminar, transitional or turbulent. In a laminar flow, the fluid elements move along smooth paths and in separate layers (Figure 4.1(a)). In a turbulent flow, the fluid elements move along random and irregular paths with no structure [35] (Figure 4.1(b)). All turbulent flows are chaotic which means that the dynamics of fluid elements in the flow are very sensitive to their initial conditions. This makes the motion of a turbulent flow very difficult to predict. Transitional flows have features of both turbulent and laminar flows, they will not be discussed further in this thesis.

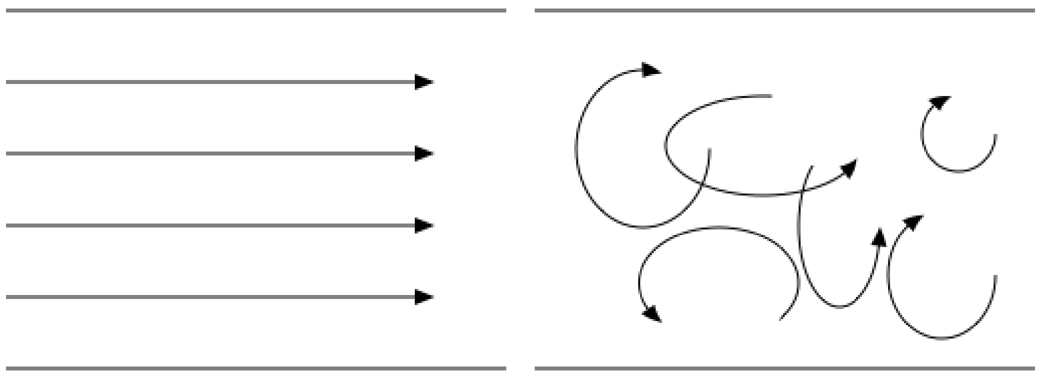

(a) Laminar flow (b) Turbulent flow

Figure 4.1: Panel a) shows the streamlines of a laminar flow, where the fluid is moving in layers without mixing. Panel b) shows the streamlines of a turbulent flow. The motion of a particle of the turbulent fluid is chaotic and it is very difficult to predict.

The difference between the dominating forces in turbulent and laminar flows can help explain the difference between them. In turbulent flows, inertial forces dominate. Inertial forces are due to the momentum of the fluid elements. When the momentum of a fluid element is high it is more resistant to changing its velocity by external forces. In laminar flows, viscous forces dominate. Viscous forces are analog to friction forces and they oppose the relative movement between neighboring fluid elements. Which one of these two forces that is dominant are determined by the Reynolds number for the fluid. The Reynolds number for a fluid describes the relative ratio between the magnitude of the inertial and viscous forces. The definition of the Reynolds number Re is

$$\mathrm{Re} = \frac{u_0 L \rho}{\mu}, \tag{4.1}$$

where u_0 denotes a characteristic flow rate and L a characteristic length scale. For the latter, it is typical to use the smallest dimension of the surroundings that confine the flow. Finally, μ and ρ are the viscosity and the density of the fluid, respectively. The Reynolds number derives from the Navier-Stokes equation. For an incompressible fluid the Navier-Stokes equation is written as

$$\rho \left(\frac{\partial \mathbf{u}(\mathbf{r},t)}{\partial t} + \mathbf{u}(\mathbf{r},t) \cdot \nabla \mathbf{u}(\mathbf{r},t) \right) = -\nabla p(\mathbf{r},t) + \mu \nabla^2 \mathbf{u}(\mathbf{r},t), \tag{4.2}$$

where $\mathbf{u}(\mathbf{r},t)$ is the velocity of the flow and $p(\mathbf{r},t)$ is the pressure in the fluid. If the flow is steady, the time variable t and time derivative of $\mathbf{u}$ can be dropped, resulting in the steady version of the Navier-Stokes equation [32]

$$\rho \mathbf{u}(\mathbf{r}) \cdot \nabla \mathbf{u}(\mathbf{r}) = -\nabla p(\mathbf{r}) + \mu \nabla^2 \mathbf{u}(\mathbf{r}). \tag{4.3}$$

The term on the left hand side is the inertial term, which determines the magnitude of the inertial forces. The diffusion term on the right hand side is the viscosity term. Eq.

(4.1) is obtained by making Eq. (4.3) dimensionless with, for example, the following change of variables:

$$\tilde{r} = \frac{\mathbf{r}}{L}, \;\; \tilde{\mathbf{u}} = \frac{\mathbf{u}}{u_0}, \;\; \tilde{p} = \frac{pL}{\mu u_0}.$$

With this change of variables Eq. (4.3) get the following appearance:

$$\frac{u_0 L\rho}{\mu}\tilde{\mathbf{u}}(\tilde{\mathbf{r}}) \cdot \nabla\tilde{\mathbf{u}}(\tilde{\mathbf{r}}) = -\nabla\tilde{p}(\tilde{\mathbf{r}}) + \nabla^2\tilde{\mathbf{u}}(\tilde{\mathbf{r}}). \tag{4.4}$$

The Reynolds number is here a scalar for the inertial term and for a flow with low Reynolds number the inertial forces are minimized. A creeping flow, the type of flow investigated in this thesis, have a Reynolds number that is far less than one ($\mathrm{Re} \ll 1$)[25].

The Reynolds number for a fluid is not to be confused with the Reynolds number Re_p for a particle. The Reynolds number Re_p is defined slightly different than the Reynolds number for a fluid,

$$\mathrm{Re}_p = \frac{v_0 d_p \rho}{\mu}. \tag{4.5}$$

Here ρ and μ are defined as in Eq. (4.1), i.e. as the density and viscosity of the fluid. The parameter v_0 is the relative velocity of the particle to the fluid and d_p is a characteristic length scale of the particle, such as the diameter of a sphere [27].

For a fluid with a low Reynolds number the inertial term can be neglected, which results in Stokes equation

$$\mu\nabla^2\mathbf{u} = \nabla p. \tag{4.6}$$

For a linear shear flow, the pressure gradient ∇p is equal to zero and equation 4.6 is reduced to

$$\mu\nabla^2\mathbf{u} = 0, \qquad \nabla\mathbf{u} = \begin{bmatrix} 0 & \mathrm{s} & 0 \\ 0 & 0 & 0 \\ 0 & 0 & 0 \end{bmatrix}, \tag{4.7}$$

where s is a constant called the shear strength. The shear strength can be seen as the slope of the dotted line in Figure 4.2(a).

The flow in the experiments for this thesis is not linear since it is pressure driven by a syringe pump. This means that the pressure gradient ∇p is nonzero and the solution of $\mathbf{u}$ in Eq. (4.6), differs from the flow profile assumed by Jeffery. The solution $\mathbf{u}(\mathbf{r})$ for a pressure driven flow, if it is considered to be between two parallel plates with infinite extent, is a Poiseuille shear flow. It has a quadratic flow profile, shown in Figure 4.2(b).

For spheroidal and cylindrical particles, Chwang [10] and Ingber and Mondy [22] have both concluded that the orientional dynamics in a quadratic flow are the same as in the case of a linear shear flow. There is no evidence, to the knowledge of the author, to whether or not this is true for the case of non-axisymmetric particles. However, in the analysis of the experiments, due to the small dimensions of the microrods, the shear can be assumed to be locally linear. This is motivated by the fact that the lengths of the microrods are small in comparison to the depth of the channel (Figure 4.2).

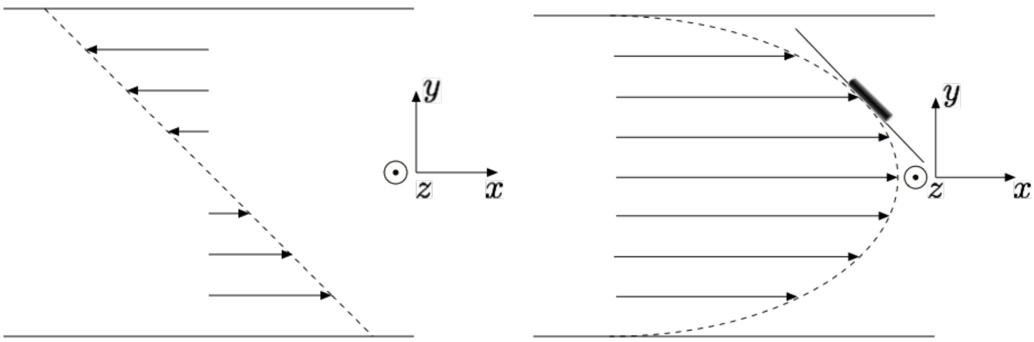

(a) Linear shear flow

(b) Poiseuille shear flow profile

Figure 4.2: Panel a) shows a linear shear flow, where the shear is in the $y-$direction. The shear strength s is the change in flow rate along the shear direction. It can be seen as the slope of the dashed line. Panel b) shows the flow profile of a Poiseuille flow. Due to the small dimensions of a microrod in comparison to the curvature of the Poiseuille flow, the shear around a rod can be seen as locally linear.

4.2 Aspect ratio and asymmetry

An ellipsoid is usually defined by three semi-axes (a,b,c). However, the orientational motion of an ellipsoid, determined by Jeffery's equations, is only dependent on the relative difference between the three semi-axes. Hence, it is sufficient to know its aspect ratio and asymmetry. Denoting the major semi-axis of an ellipsoid with a and the minor semi-axis by b, ($a > c \geq b$), the aspect ratio is defined as

$$\lambda_e = \frac{a}{b}. \tag{4.8}$$

Equivalently for a cylindrical rod, denoting the length by L_{rod} and the diameter by d_{rod}, the aspect ratio is defined as

$$\lambda_{\text{rod}} = \frac{L_{\text{rod}}}{d_{\text{rod}}}. \tag{4.9}$$

Both relations are illustrated in Figure 4.3.

The asymmetry ε for an ellipsoid is defined as the relative difference between the minor and medium semi-axes,

$$\varepsilon = \frac{c}{b} - 1. \tag{4.10}$$

The asymmetries of the cylindrical microrods used in the experiments are more complex since they originate from random irregularities at the rod ends. A very important difference between the asymmetry of an ellipsoid and that of a rod is that there are rarely any axes of symmetry due to these irregularities, as shown in Figure 4.3, while a non-axisymmetric ellipsoid has three. It is not known how the absence of symmetry-axes of the rods affects their orientational dynamics.

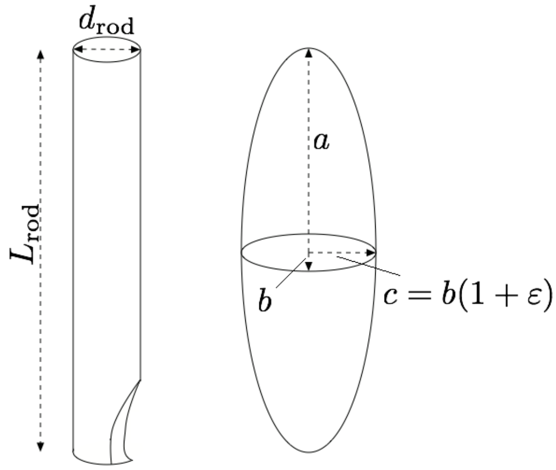

Figure 4.3: The figure shows how the dimensions of the two types of particles are defined. The aspect ratio of an ellipsoid is defined as $\lambda_e = a/b$ and the asymmetry as $\varepsilon = c/b - 1$. Equivalently, the aspect ratio of a cylindrical rod is defined as $\lambda_{\text{rod}} = L_{\text{rod}}/d_{\text{rod}}$. The asymmetry for the cylindrical microrods originates from random irregularities at the rod ends and it is very difficult to define in mathematical terms. A non-axisymmetric ellipsoid has three axes of symmetry, while an asymmetric rod rarely has any.

4.3 Jeffery's equations of motion

Jeffery [23] derived equations of motion for an arbitrary triaxial ellipsoid. Using similar notation as Yarin *et al.* [41], Jeffery's equations take the form:

$$\frac{d\theta}{dt} =(g_2 \sin\psi + g_3 \cos\psi)\sin\theta, \tag{4.11a}$$

$$\frac{d\phi}{dt} =\frac{1}{2} + g_3 \sin\psi - g_2 \cos\psi, \tag{4.11b}$$

$$\frac{d\psi}{dt} =g_1 + (g_2 \cos\psi - g_3 \sin\psi)\cos\theta, \tag{4.11c}$$

where t is dimensionless. Here g_1, g_2, g_3 are also functions of θ, ϕ and ψ. They are given by

$$g_1 =\frac{b^2-c^2}{2(b^2+c^2)}[-\frac{1}{2}(\cos^2\theta+1)\sin 2\phi \sin 2\psi + \cos\theta \cos 2\phi \cos 2\psi], \tag{4.12a}$$

$$g_2 =\frac{c^2-a^2}{2(a^2+c^2)}[-\cos\theta\sin 2\phi \sin\psi + \cos 2\phi \cos\psi], \tag{4.12b}$$

$$g_3 =\frac{a^2-b^2}{2(a^2+b^2)}[\cos\theta\sin 2\phi \cos\psi + \cos 2\phi \sin\psi]. \tag{4.12c}$$

The angles θ, ϕ and ψ are the Euler angles, where θ and ϕ describe the orientation of the major semi-axis of the ellipsoid, shown in Figure 4.4. The angle ψ describes the rotation of the ellipsoid around its major semi-axis. The constants a, b and c are the lengths of the semi-axes of the ellipsoid, shown in Figure 4.3. The axes ($\tilde{x}$,$\tilde{y}$,$\tilde{z}$) in Figure 4.4 describe the reference system used by Yarin *et al.* [41], while the axes (x,y,z) describe the reference system used in the experiments described in this thesis.

It is worth to notice that the shear strength s of the linear shear flow does not occur anywhere in Eqs. (4.11) or (4.12). This is because it is included in the dimensionless time variable t [41].

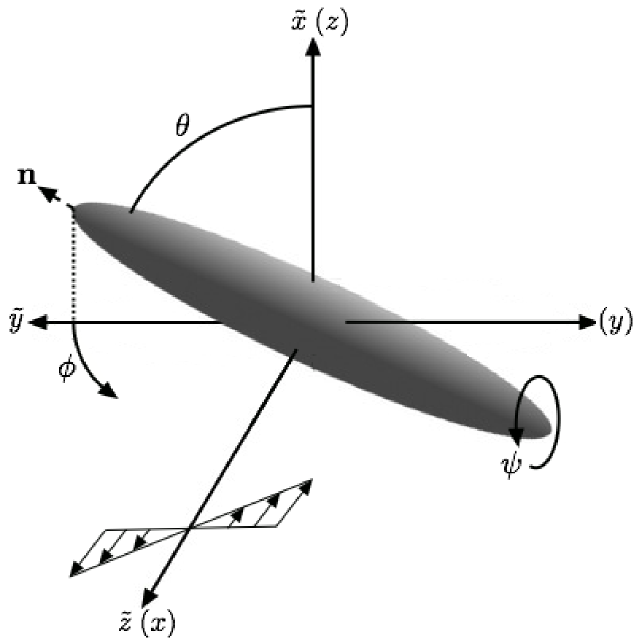

Figure 4.4: The flow points in the direction of the $\tilde{z}$-axis (x-axis). The coordinate system ($\tilde{x}$,$\tilde{y}$,$\tilde{z}$) denote the frame of reference used by Yarin *et al.* [41]. (x,y,z) are the frame of reference used for the experiments. **n** denotes the orientation-vector of the major semi-axis. (θ,ϕ,ψ) = (0,0,0) corresponds to when the major semi-axis of the ellipsoid is aligned with the $\tilde{x}$-axis and the minor semi-axis is aligned with the $\tilde{y}$-axis.

4.3.1 Jeffery orbits

Jeffery's equations are solved with respect to the initial conditions

$$t = 0, \qquad \theta = \theta_0, \qquad \phi = \phi_0, \qquad \psi = \psi_0,$$

where (θ,ϕ,ψ) = (0,0,0) corresponds to the case where the major semi-axis of the ellipsoid is aligned with the $\tilde{x}$-axis and the minor semi-axis is aligned with the $\tilde{y}$-axis, see Figure 4.4. For spheriods (a=b=c) and axisymmetric ellipsoids (a>b=c) Eqs. (4.11) admit simple analytical solutions that were obtained by Jeffery [23]. In the case of an axisymmetric ellipsoid the solution takes the form

$$\tan\phi = \lambda_e \tan\left(\frac{ac}{a^2+c^2}t\right), \qquad \tan\theta = Ca(a^2\cos^2\phi + c^2\sin^2\phi)^{-1/2}, \tag{4.13}$$

where C is the orbit constant [41]. The solutions (4.13) form closed trajectories and they are commonly known as *Jeffery orbits*. C is called the orbit constant because it uniquely determines the orientational trajectory of a particle. Every point on the unit sphere is associated with a unique orbit. Consequently, there is an infinite number of orbits. A few examples are shown in Figure 4.5.

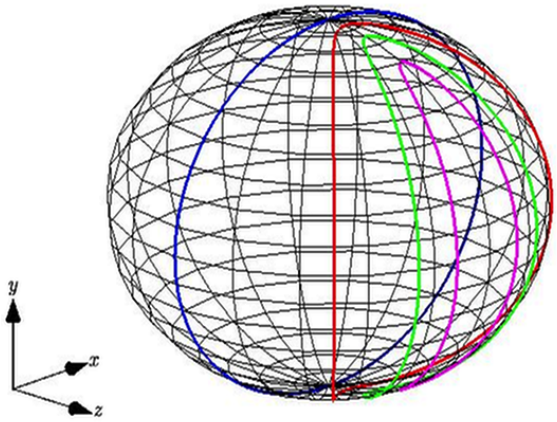

Figure 4.5: The colored trajectories are solutions to Jeffery's equations (4.13), for an axisymmetric particle. The colors correspond to solutions with different orbit constants, determined by the initial conditions.

4.3.2 Non-axisymmetric particles and Poincaré maps

The main focus of this thesis is to study the motion of asymmetric particles. For these particles, simple analytical solutions for the equations of motion do not exist in general. This is also the case for a non-axisymmetric ellipsoid. The solutions to Eqs. (4.11) can instead be analyzed using numerical methods, see [22, 41].

One way to analyze the orientational trajectory of a particle is by a Poincaré map. A Poincaré map is commonly used in the analysis of dynamical systems, it reduces the study of a trajectory to the study of a map of points through a surface in the same space as the trajectory. This surface is called the Poincaré section and the map of points obtained is called the Poincaré map. From the Poincaré map for trajectories of a particle it is possible to see how its orientation changes [39].

For a particle whose motion is governed by Jeffery's equations, Hinch and Leal [21] proposed to study the dynamics of the Poincaré map for θ and ψ. They further suggested to choose the Poincaré section $\phi = n\pi$ since this guarantees that the Poincaré section covers all possible trajectories.

The Poincaré maps in Figure 4.6 were generated by numerically integrating modified versions of Eqs. (4.11) for different initial conditions with ϕ as the integration variable, (see appendix A). The values of θ and ψ are sampled at $\phi = n\pi$. Figure 4.6 a) - f) show how the orientational dynamics for an ellipsoid change with an increase in the asymmetry parameter ε.

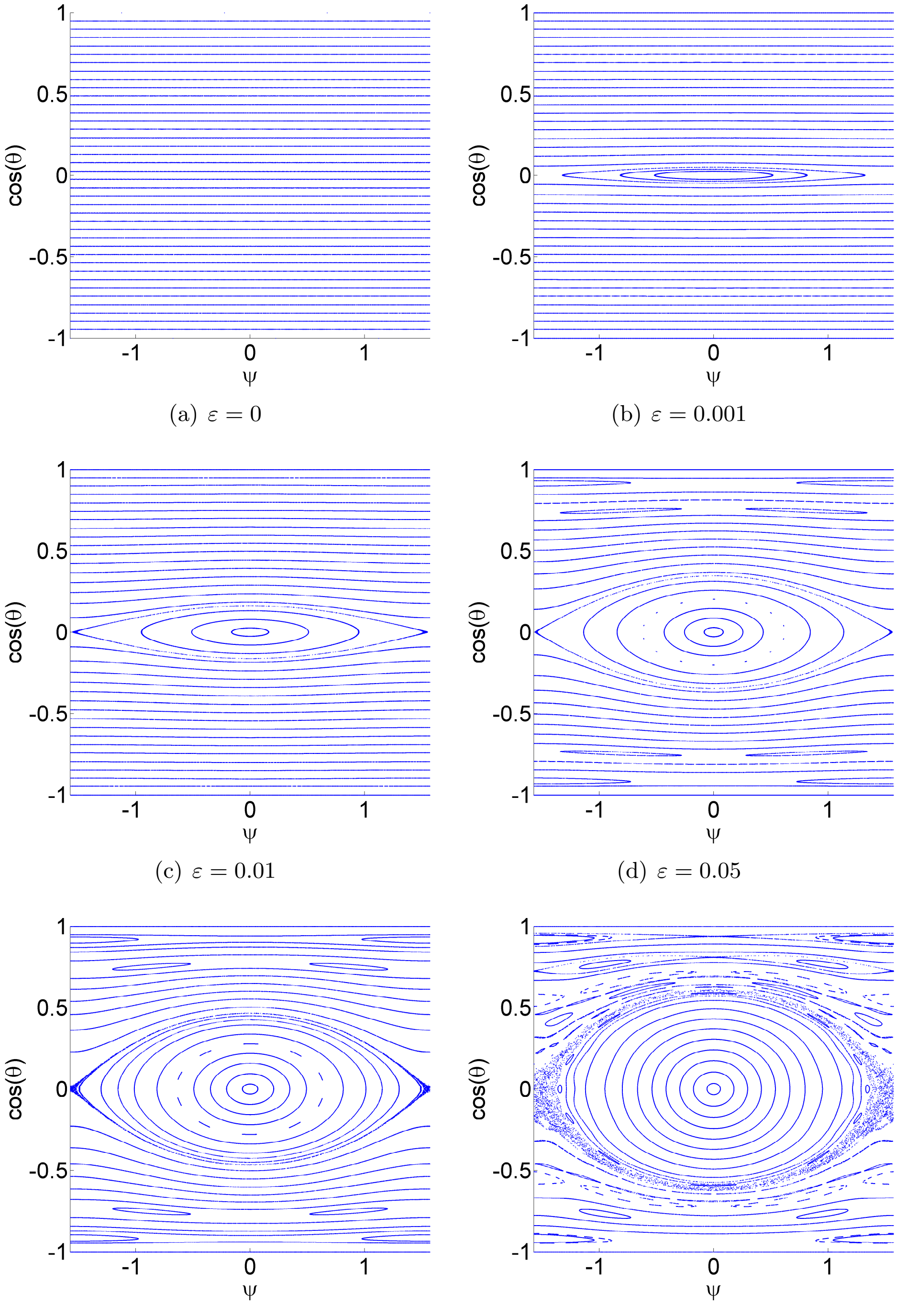

(a) $\varepsilon = 0$ (b) $\varepsilon = 0.001$

(c) $\varepsilon = 0.01$ (d) $\varepsilon = 0.05$

(e) $\varepsilon = 0.1$ (f) $\varepsilon = 0.2$

Figure 4.6: Different panels show Poincaré maps for different asymmetries ε. Each map contains data from different initial conditions. It is obvious from the figures that an increase in asymmetry changes the orientational dynamics of a particle. The angle ψ is expressed in radians and it is mapped to the interval [-π,π] by asin(sin ψ).

For axisymmetric ellipsoids $\cos\theta$ is a constant of motion for every initial condition, (Figure 4.6(a)). Trajectories where $\cos\theta$ is a constant of motion in the Poincaré map are referred to as periodic trajectories. The angle ψ, for an axisymmetric particle, is irrelevant since it describes the orientation around the major semi-axis.

For non-axisymmetric particles tori start to appear in the Poincaré map. Even for an asymmetry ε as small as 0.001 tori appear in the center of the map. With increasing asymmetry the tori extends from the center towards the edges of the map. Outside the tori there are traces that are curved. Trajectories that generate tori and traces that are curved are referred to as quasi-periodic trajectories. It should be noticed that even for high asymmetries, at the edge of the Poincaré map, $\cos\theta$ is still a constant of motion as in the case of axisymmetric particles.

For ellipsoids with higher asymmetries an additional region arise in the Poincaré map. In Figure 4.6(e) the region is quite narrow. The points in this region do not have any noticeable trace. Instead the points look smeared out. The region extends with higher asymmetries and is more apparent in Figure 4.6(f). This region is a chaotic layer [41], but it is not discussed in this thesis.

4.3.3 Winding number

The aspect ratio of a particle affects the frequencies of the orientational dynamics. However, this effect is hard to distinguish in the Poincaré map since it does not noticeably change its appearance. For an axisymmetric particle the trajectories follow closed orbits since θ and ϕ have the same period. The frequency of the dynamics can in this case be measured by the period of the rotation around this orbit. For non-axisymmetric particle where the motion is quasi-periodic, the frequencies of the different orientational dynamics differ and it is in this case more convenient to describe the frequency of the system with the winding number. The winding number is defined as [15]

$$W = \lim_{n\to+\infty} \frac{\gamma_n - \gamma_0}{n}. \tag{4.14}$$

For the winding number of the orientational motion of an triaxial ellipsoid, n connected to frequency of the ϕ-angle i.e. it is the number of periods $n\pi$ of ϕ. The γ-angle is connected to the frequencies of the angles θ and ψ. From a starting point p_0 in the Poincaré map, the angle γ_0 is defined as $\arg(p_0)$. For the periodic trajectories, where $\cos\theta$ is a constant of motion, the angle γ can is described only by ψ. For the tori it equals $\arg(\psi, \cos\theta)$. Further, if f is the mapping function for the Poincaré map from one point to the next, $p_1 = f(p_0)$, the point p_n is obtained as $p_n = f^{(n)}(p_0)$ and $\gamma_n = \arg(p_n)$. The winding number can be seen as the average incremental of the argument for the points $p_0, ..., p_n$ when n goes to infinity [15]. The difference in frequencies of the orientational dynamics for two particles with two different aspect ratios is shown in Figure 4.7.

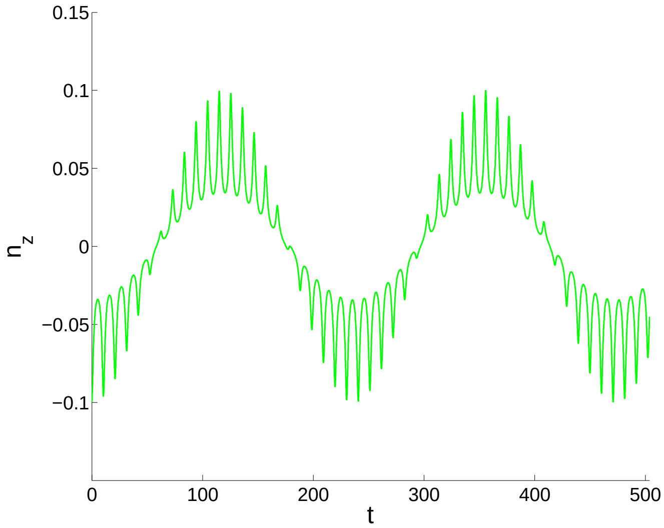

(a) $\lambda_e = 3$

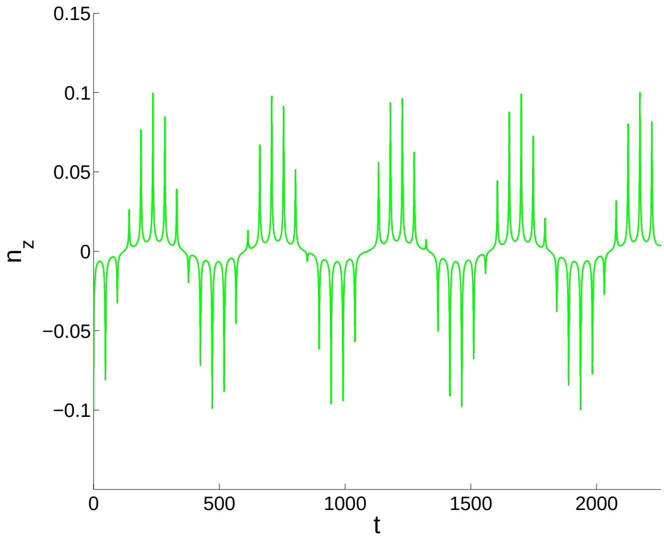

(b) $\lambda_e = 15$

Figure 4.7: The figure shows how the frequencies of the system change with the aspect ratio. Both particles have an asymmetry of 0.05 and they are generated from the same initial condition. As seen the frequency of the amplitude in comparison to the frequency of the peaks is a lot lower for the particle with the smaller aspect ratio (Panel a)). The winding number for the trajectory in Panel a) is lower than for the one shown in Panel b).

4.3.4 Analysis of the the orientation-vector components

The Euler angles are difficult to observe directly in the experiments and the angle ψ is not observable at all. Therefore, the orientational motion of a particle is instead analyzed by the components of its orientation-vector

$$\mathbf{n}(t) = \begin{pmatrix} n_x(t) \\ n_y(t) \\ n_z(t) \end{pmatrix}, \tag{4.15}$$

normalized to unity. The relations between the $\mathbf{n}(t)$-components and the Euler angles are

$$\begin{aligned} n_x &= \sin\phi\, \sin\theta, \\ n_y &= \text{-}\cos\phi\, \sin\theta, \\ n_z &= \cos\theta, \end{aligned} \tag{4.16}$$

as shown in Figure 4.4. The trajectories in Figure 4.5, presented as the times series of $\mathbf{n}(t)$, are shown below in Figure 4.8.

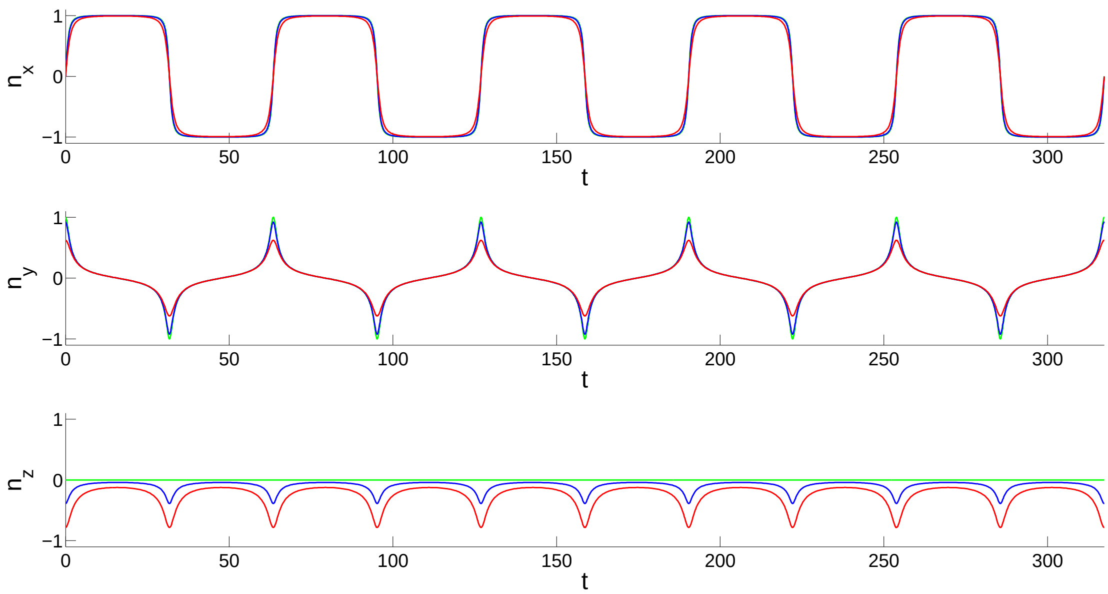

Figure 4.8: The figure illustrates the Jeffery orbits in Figure 4.5 as time series of $n_x(t)$, $n_y(t)$, $n_z(t)$.

Examples for time series of quasi-periodic motion are shown in Figure 4.9. The relation between the time series of $\mathbf{n}(t)$ and a Poincaré map can be seen by noticing that the n_z component is calculated as $\cos\theta$, the same as the vertical axis of the Poincaré map. Each point in the Poincare map is sampled when $\phi = n\pi$. From Eq. (4.16) this means that the values on the vertical axis in the Poincaré map are the values of n_z when n_x equals to zero. For small asymmetries ε, the values on the vertical axis in the Poincaré map are very close to the peak values of n_z.

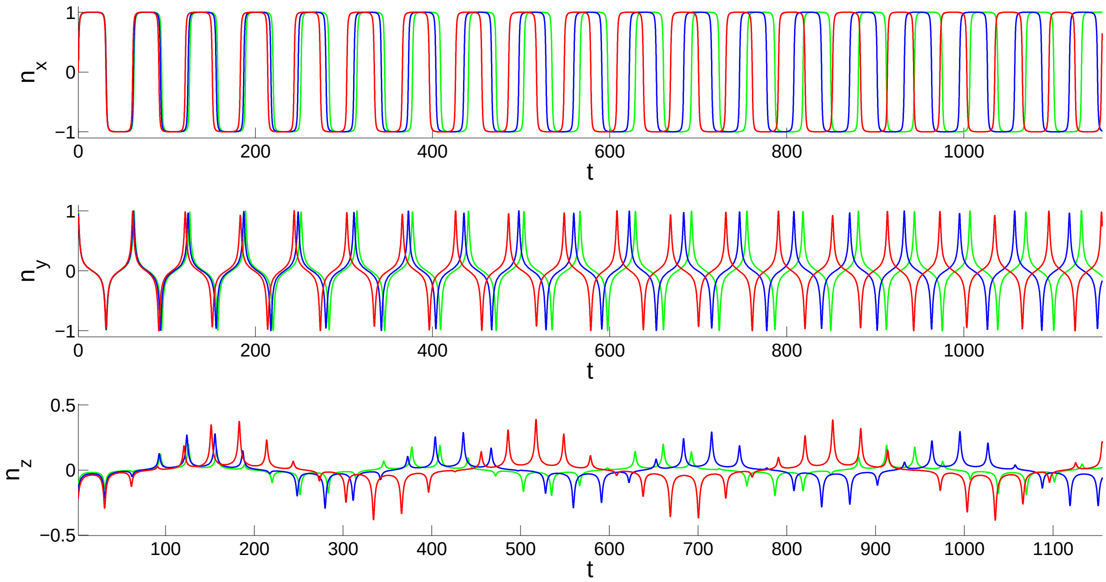

Figure 4.9: The figure shows time series for a particle with aspect ratio of $\lambda_e = 7$ and an asymmetry of $\varepsilon = 0.1$. There is a slight drift in amplitude between each peak. This is most obvious when looking at the time series for n_z, (notice the scale on the n_z-axis). The time series correspond to tori in Figure 4.6(e). Different colors correspond to different initial conditions.

5

Method

THIS chapter describes how the measurements and analysis of the orientational motion of a particle are carried out. The experiments are a continuation of the previous work of [12, 24, 30] and most of the experimental setup is the same. In the previous experiments, polymer fibers were used. Their shapes were irregular and hard to determine. In the experiments carried out for this thesis, the polymer fibers are replaced by cylindrical microrods made of glass with a very precise diameter. However, the new particles have forced some unwanted changes to the experimental setup. With the polymer fibers it was possible to use pure glycerol as the surrounding fluid. Glycerol is transparent and highly viscous. The microrods have a density that is significantly higher than that of the polymers and it is therefore not possible to use only glycerol as the working medium. A new fluid, consisting of a mixture of water, glycerol and sodium metatungstate monohydrate, is therefore used. The latter is a substance with high density, for the purpose of compensating for the density of the microrods. The mixture is less viscous than glycerol and it is also less transparent.

The data analysis is performed in Matlab. The data is extracted by the software developed by Johansson [24] to which only some minor changes are made. Also, additional software to analyze the reversal and drift of a particle are developed together with a numerical method to compare the experimental data with the orientational motion of an ellipsoid, derived from Jeffery's equations. Previously this comparison was performed manually by comparing the plots of the experimental data with plots of theoretical trajectories.

5.1 Experimental setup

The flow and particles are studied in a microfluidic channel made of PDMS, which is a silicon organic-based polymer well recognized for its use in microfluidic systems due to its physical properties. The microfluidic channel has the dimensions $40 \times 2.5 \times 0.14$mm. It has two inlets and it is sealed with a 0.17mm thick cover slip made of glass. A thicker cover slip makes the channel more stable, however, the microscope objective is calibrated for the thin cover slip and a thicker one compromises the quality of the optical tweezers.

One of the inlets is connected to a syringe through a PTFE -tubing. The syringe in turn is connected to a pump. The other inlet is connected to a beaker with a buffer of the fluid. When setting up the experiment all visible air bubbles are removed from the microchannel and the tubing. In particular, bubbles in the channel are noticed to affect the motion of the fluid.

The channel is mounted on a movable stage over the 60x water immersion objective. The syringe pump has both infusion and withdrawal functionality and it is used to control the direction and velocity of the flow. A CCD camera is used to record the particles, see Figure 5.1.

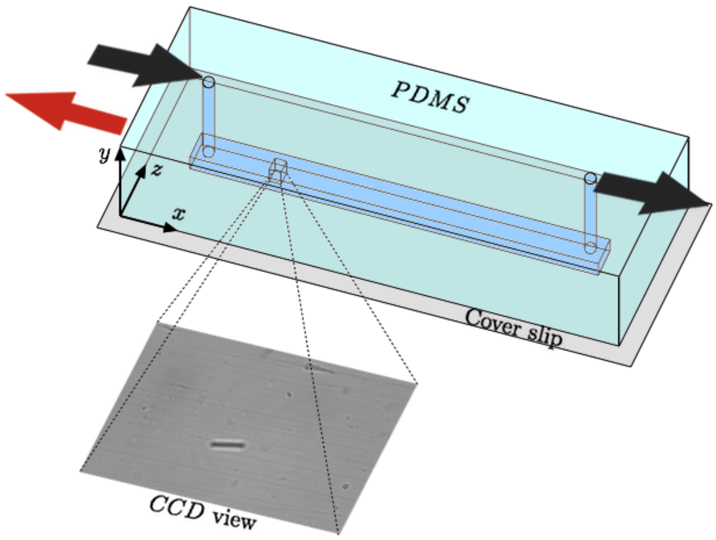

Figure 5.1: The particles are recorded with a CCD camera. When using a high-resolution objective, the field of view is very small compared to the length of the micro channel. The channel is therefore mounted on moveable stage to be able to track the particles as their position change. The black arrows indicate the direction of the flow, while the red arrow indicates how the position of the channel is changed by the movable stage to follow the particle for the given flow direction.

Before the flow is started, the optical tweezers position a microrod at a suitable depth and orientation. When the pump starts the flow, the CCD camera starts to record the motion of the microrod. When the rod approaches one of the inlets the flow is reversed. The data obtained between two reversals is said to belong to a stretch. For every initial condition a number of consecutive stretches are recorded and the collected data for each initial condition is called a measurement. At the end of a measurement, the flow is stopped and the initial conditions of the microrod are changed. For each microrod several measurements are made with varying initial conditions.

5.1.1 Microrods

The particles used in the experiments are cylindrical microrods made of glass. They have a precise diameter of 3μm but their length varies. Detailed images of the microrods were taken using a SEM-microscope[1] (sweeping electron microscope) to see how their shape varies. The result is shown in Figure 5.2[2].

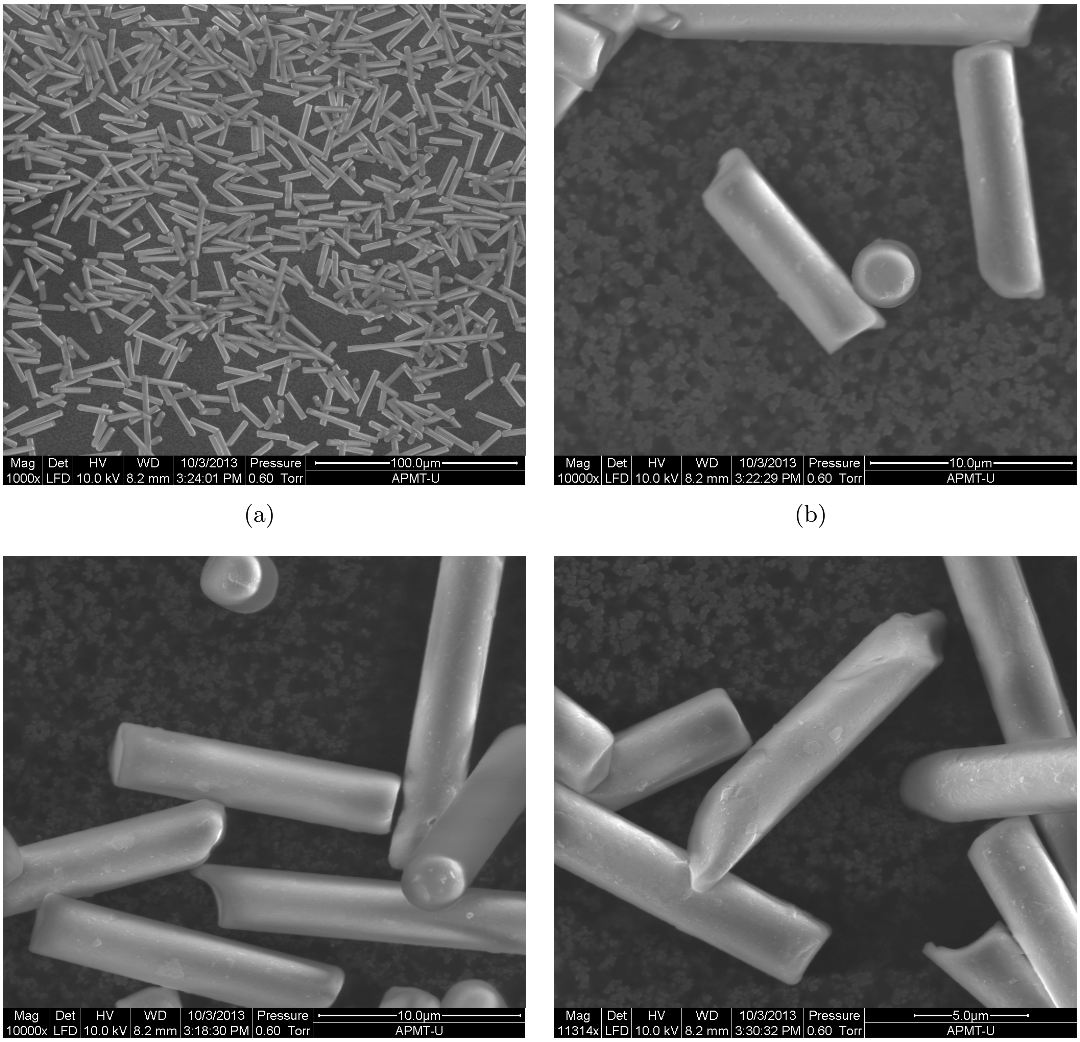

(a) (b) (c) (d)

Figure 5.2: The figures show how both the length and asymmetry of the microrods varies. The mircorods have a very precise diameter of $3\mu m$.

[1]The images were taken with help from Stefan Gustafsson of the Eva Olsson Group at Chalmers University of Technology.

[2]Figure b) and c) are the same figures as Figure 3.7b) and 3.7a) in the thesis of Ankardal [2], respectively.

As described in Section 4.3.2 the orientational motion of an ellipsoid is highly dependent on its asymmetry ε. This is also expected for the motion of cylindrical particles. To study the different types of orientational motion of cylindrical microrods it was therefore important to see that the asymmetry varies. As seen in Figure 5.2 there are examples of microrods with both high and low asymmetry.

5.1.2 Fluid

The fluid is mixture of water, glycerol and sodium metatungstate monohydrate (SMTS). The SMTS is used to match the density of the fluid to the density of the microrods, which have a specied density of 2.56g/cm^3. SMTS is a wolfram-based substance with a maximum density of 3.04g/cm^3, when dissolved in water. Water has a density around 1.00g/cm^3 and glycerol has a density of 1.26g/cm^3. A mixture with volume consisting of 74.5% SMTS, 16.5% water and 9% glycerol, was found to match the density of the microrods. The density match is very important, a deviation as small as 1-2% causes the particles to drift noticeably in the y-direction of the channel.

The glycerol is added to increases the viscosity of the fluid. With the mentioned concentrations the fluid has a viscosity of 25.0mPa s, (measured with a Rheometer[3]). This can be compared to water that has a viscosity of 1.002mPa s and to glycerol with a viscosity of 1.408Pa s. (All mentioned viscosities are valid for 20°C [40], which is the temperature of the lab).

5.1.3 Reynolds numbers Re and Re_p

Jeffery's equations are valid under the assumption that the particles are inertialess and the flow is creeping. This means that the Reynolds number is close to zero for both.

With the pump set to run at 7.5μl/min, which equals a maximum velocity of approximately 0.66mm/s in the center of the microchannel, a depth of the microchannel of 140μm, a density of the fluid of 2.56g/cm^3 and viscosity of 25.0mPa s the Reynolds number for the flow is in the order of

$$\mathrm{Re} = \frac{0.66 \cdot 10^{-3} \cdot 140 \cdot 10^{-6} \cdot 2.56 \cdot 10^{3}}{0.025} \frac{\mathrm{m/s} \cdot \mathrm{m} \cdot \mathrm{kg/m^3}}{\mathrm{kg/m\,s}} = 9.36 \cdot 10^{-3},$$

which sufficiently satisfies the creeping condition for the flow [25].

The Reynolds number for the microrods is calculated using the diameter of the rods as the length parameter. The diameter is 3μm and by making an overestimation of a microrods relative velocity to the fluid v_0, by setting it to the same as the maximum flow velocity u_0, the Reynolds number Re_p becomes in the order of

$$\mathrm{Re}_p = \frac{0.66 \cdot 10^{-3} \cdot 3 \cdot 10^{-6} \cdot 2.56 \cdot 10^{3}}{0.025} = 2 \cdot 10^{-4}.$$

This means that the inertial effects upon the orientational dynamics of the particles can be neglected.

[3]The viscosity was measured at the Department of Chemistry and Molecular Biology with the help of Johan Bergenholz

5.2 Data analysis

The movie recordings from the CCD-camera contain 2D-projections of the microrods motion in the x-z-plane. To extract the orientational motion of a particle, the analysis program makes an elliptic fit to the projection in each frame of a recording. From the elliptic fit an estimated length l and angle α are obtained, see Figure 5.3.

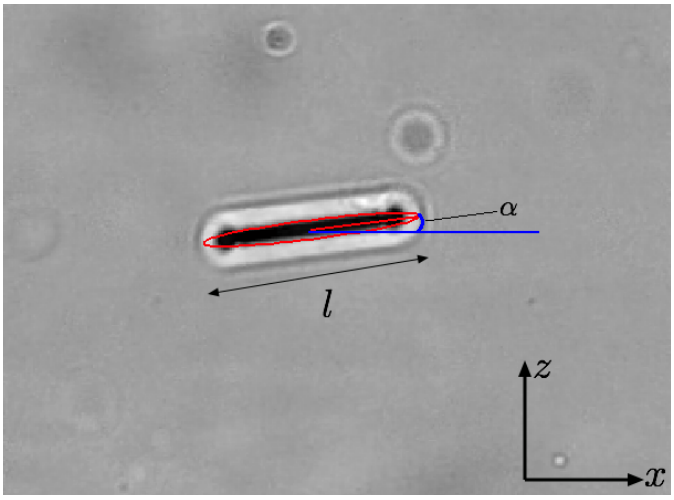

Figure 5.3: The figure shows the elliptic fit made by the analysis program. An angle α is extracted as the angle between the x-axis and the major semi-axis of the fitted ellipse. An estimated length l and a width d of the projection are also obtained by the semi-axes of the ellipse.

In order to obtain the unit components n_x and n_z, the full length of a microrod needs to be known. Conveniently, Hinch and Leal [21] noted that particles in a linear shear flow spend most of their time aligned with the flow. Assuming that this is also the case for cylindrical particles, the most frequently observed length l from the elliptic fitting should be the best estimation of the actual microrod length. By establishing a histogram over the fitted lengths l, see Figure 5.4, an estimated length of the particle L_{rod} is obtained.

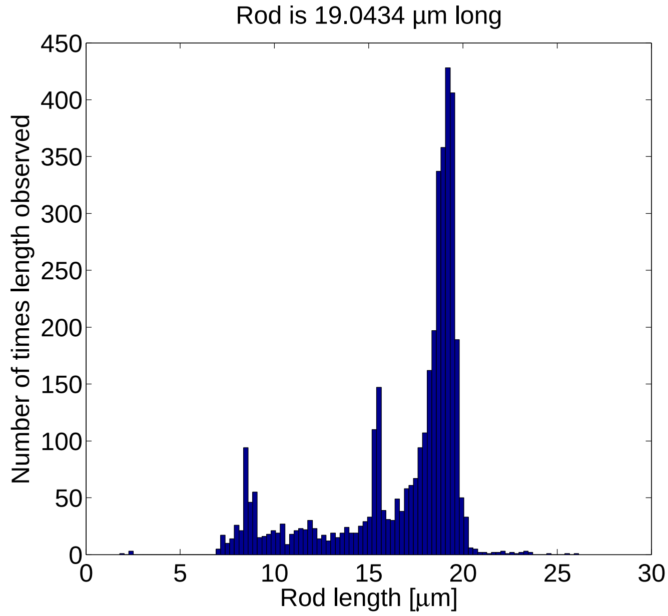

Figure 5.4: The histogram shows the distribution of the observed particle lengths l during a measurement. Since a particle spends most of its time aligned with the flow the most occurring length is the best approximation of the particle length L_{rod}.

When the length l and angle α of the elliptic fit for each frame are known, together with the estimated particle length L_{rod}, the n_x and n_z components are calculated as

$$\begin{aligned} n_x =& \frac{l\ \sin\alpha}{L_{\mathrm{rod}}}, \\ n_z =& \frac{l\ \cos\alpha}{L_{\mathrm{rod}}}. \end{aligned} \tag{5.1}$$

The n_y component can be extracted implicitly from the data since the length of the $\mathbf{n}(t)$-vector equals to one. Since the n_y-component is not directly observable it is left out of the analysis.

5.2.1 Removing the time dependency

When the pump reverts the flow the direction of both the flow rate $\mathbf{u}$ and the pressure gradient ∇p change. This reversion is performed smoothly in order to avoid inertial effects on the particle. Despite this, the flow rarely changes direction without pressure fluctuations. This in turn leads to fluctuations in the velocity. The syringe pump controls the velocity and direction of the flow and the reversing of the flow are performed in 4 steps. The first step halves the velocity, the second one turns off the pump completely, the third one reverts with half of the maximum velocity and the forth and last step set the velocity of the pump at a maximum in the reverted direction. Each of the steps 1-3 is performed during 10 seconds. An example of the velocity of a particle is shown in Figure 5.5.

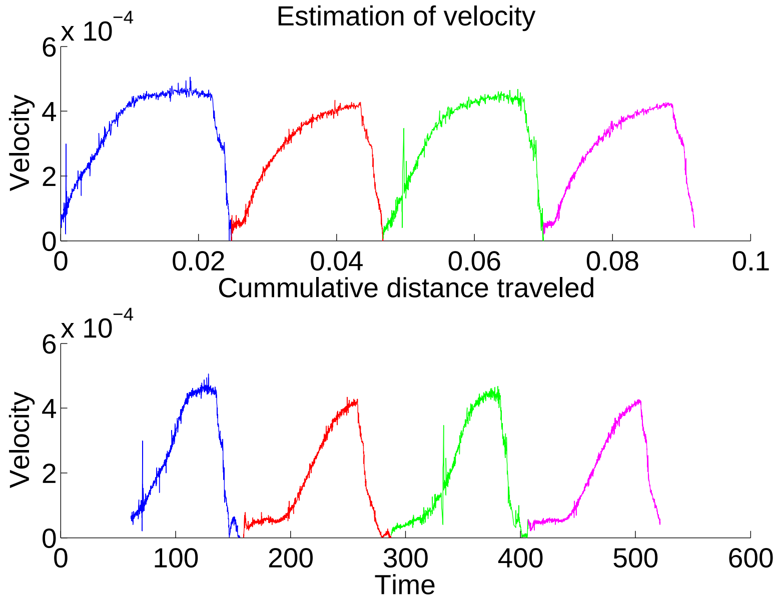

Figure 5.5: The figure shows the magnitude of the velocity in the x-direction of the microchannel for 4 stretches. At the first and third reversal the pump changes from infusion to withdrawal, while the second one shows the opposite change.

If the pressure fluctuations are without transients, both the shear strength s and velocity $\mathbf{u}$ scale linear with ∇p [12]. By plotting the components of $\mathbf{n}(t)$ against the distance traveled $x(t)$ instead of time the visible effects of the pressure fluctuations are minimized. Figure 5.6 present the orientational motion of a particle, both as a function of time, $\mathbf{n}(t)$, in Figure 5.6(a), as well as a function of distance, $\mathbf{n}(x(t))$, in Figure 5.6(b). As shown in the figures the peaks of both n_x and n_z get a constant period as a function of distance.

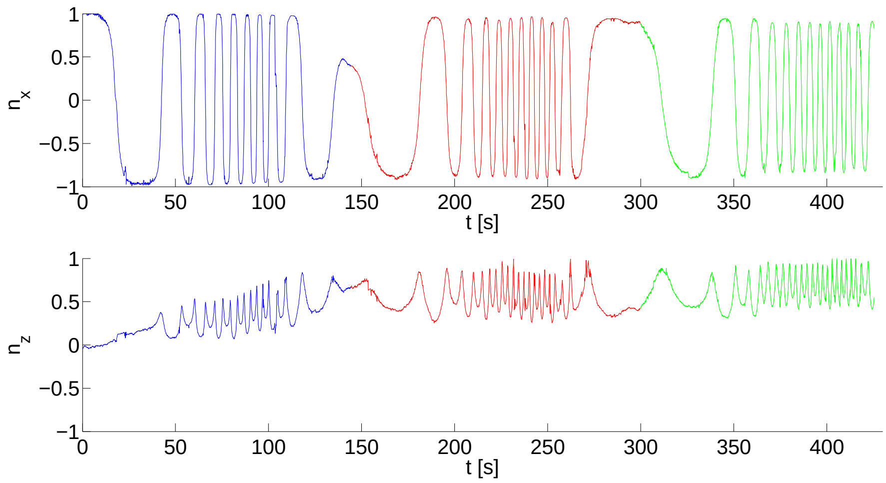

(a)

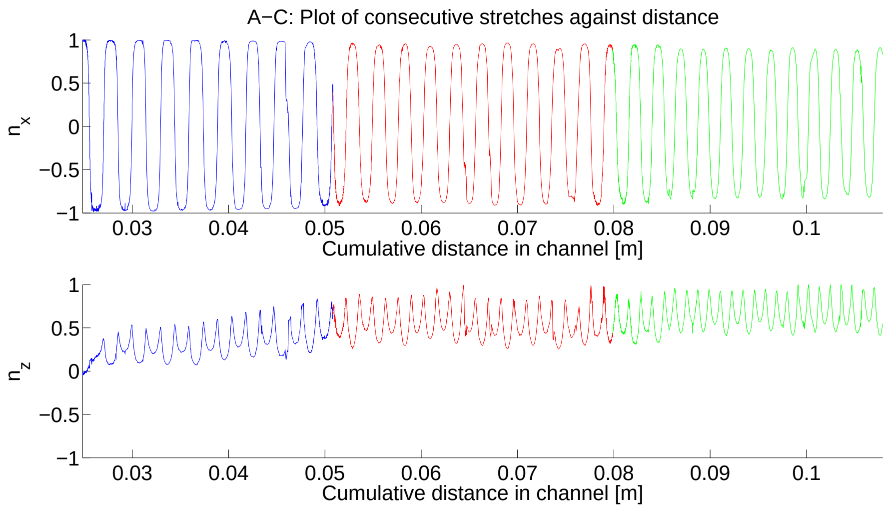

(b)

Figure 5.6: The figures show the difference between plotting the normal components n_x and n_z against time versus distance traveled. When the orientation-vector $\mathbf{n}$ is plotted against the distance, small non-transient pressure fluctuations are canceled. Panel a) shows n_x and n_z when plotted against time t. Panel b) shows them plotted against the distance traveled $x(t)$.

5.2.2 Correcting the results of image tracking

The tracking program that extracts a particles motion is not flawless and some manual correction to the extracted data is needed. The tracking can momentarily loose a particle or overestimate its length due to low contrast difference to the background. This creates tracking errors that are easy to spot by examining the data in a plot. From the plot these errors are corrected manually. An example of this is shown in Figure 5.7. The data is cross checked with the recorded movies to avoid removal of valid data points.

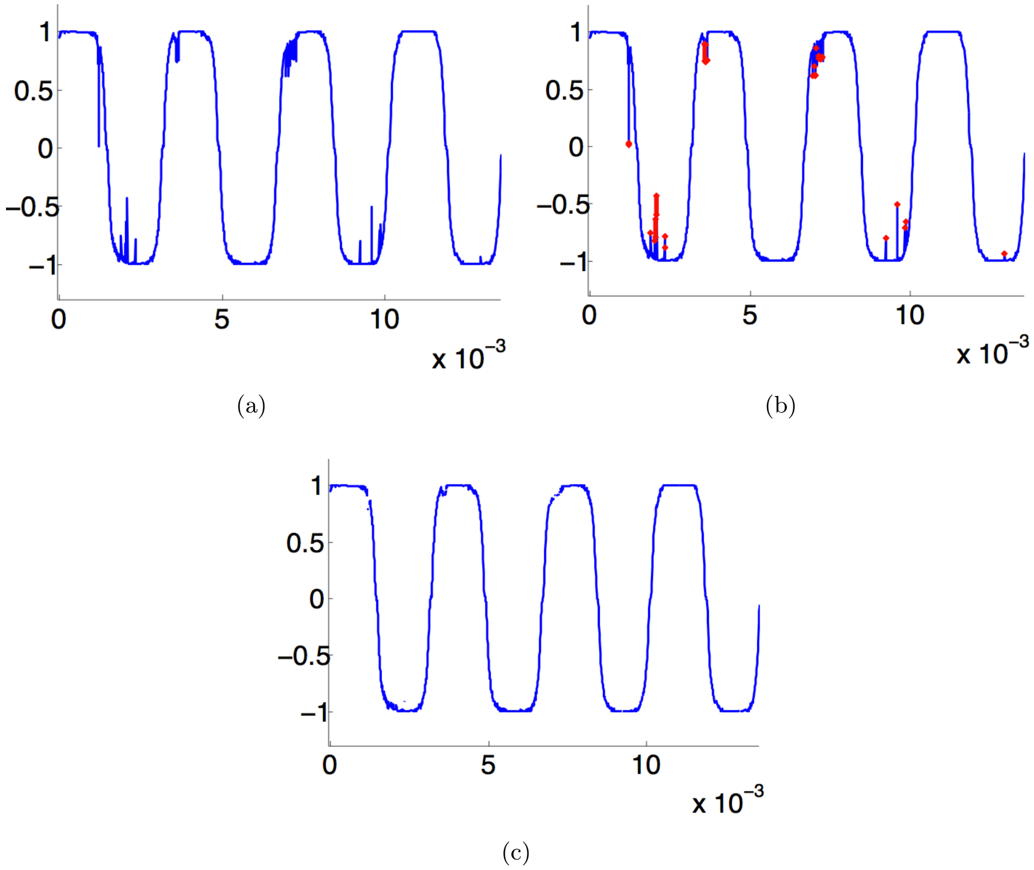

(a) (b) (c)

Figure 5.7: The figures show how false data points are removed. Panel a) shows the original data points obtained from the tracking. In panel b) the false data points are marked in red. Panel c) shows the final data where the false data points are removed.

5.2.3 Absence of inertial effects

One of the key assumptions for the experiments is that the flow and particles are inertia-less. The absence of inertial effects is controlled by analyzing the trajectory of a particle before and after the reversing of the flow. In absence of inertial effects, it is expected that the particles retrace their trajectories after the reversal. An example of a particle that successfully retrace its trajectory after the reversing of the flow and an example of a particle that does not are shown in Figure 5.8.

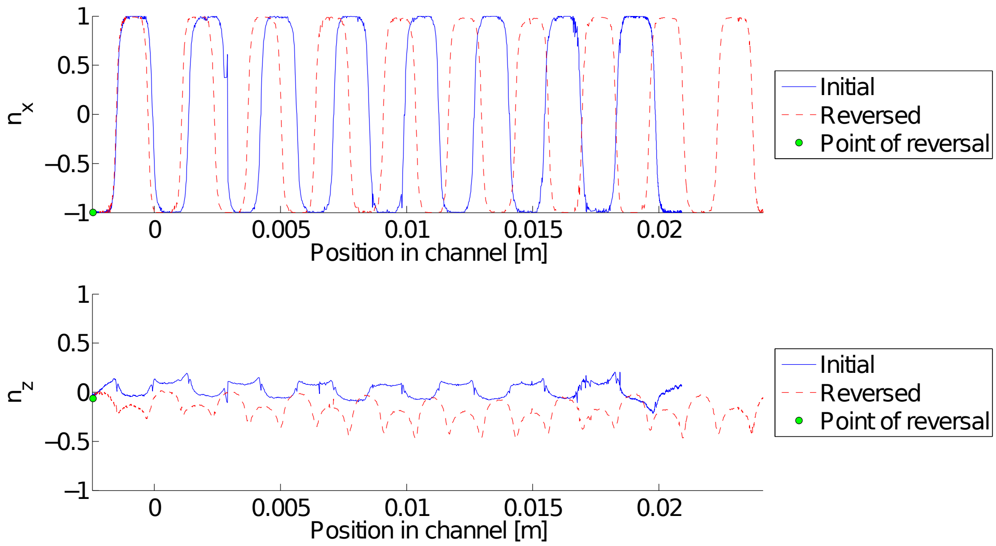

(a) Unsuccessful reversal

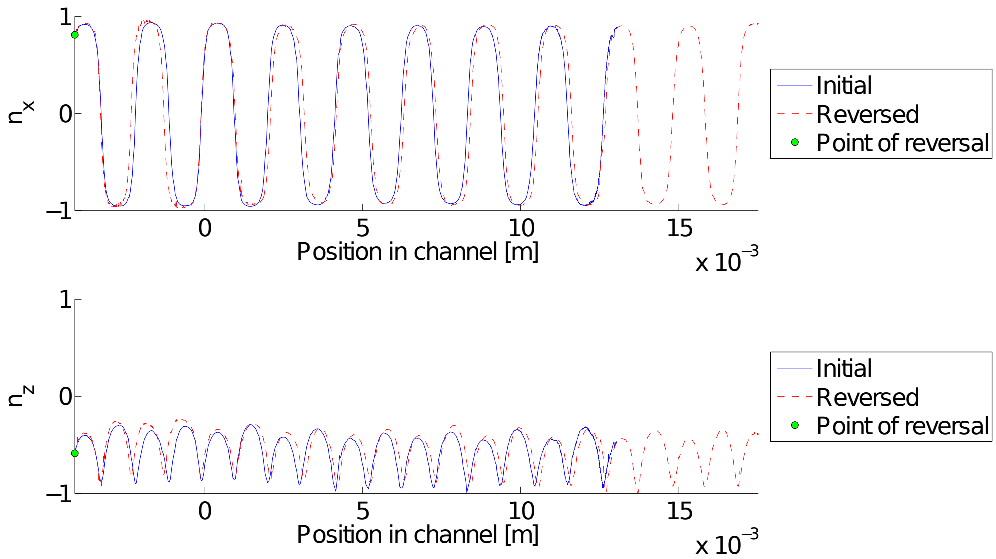

(b) Succesful reversal

Figure 5.8: The figure shows an example of two trajectories of a particle before and after a reversal. Panel a) shows a reversal where the trajectory of the particle changes completely. Panel b) shows a particle that successfully retraces its trajectory after the reversal.

5.2.4 Drift in the channel

The drift of the center of mass of the particles both in the y- and z-directions of the flow are measured. Drift in the y-direction occurs due to poorly matched densities between the fluid and particles. This drift is the most frequent problem in the measurements and it is not completely known how it affects the dynamics of a particle. Therefore, measurements for particles that drift too much are rejected.

The drift in the y-direction is measured in two ways. First, it is possible to study how the focus of a particle changes when the fluid is resting. If the focus barely changes with time it means that the density match is good since the particle stays buoyant. The second way is by measuring the change in period for n_x. According to Jeffery [23], the period is inversely proportional to the shear strength s,

$$T \propto \frac{1}{s}.$$

The difference in shear strength between different sections of the microchannel is known, it is zero in the center of channel and reaches its maximum at the walls, see Figure 4.2(b). When a particle drifts along the y-direction, the shear strength s experienced by the particle, therefore changes. Since the change in shear strength affect the period of the orientational dynamics and the change in period then gives an indication in what direction a particle is drifting. However, since the period T is disturbed by pressure fluctuations as described in Section 5.2.1, the period is calculated in terms of the distance traveled $x(t)$ instead of time,

$$\Delta x(t) = x_{i+1}(t) - x_i(t),$$

where $x_i(t)$ and $x_{i+1}(t)$ denote two consecutive points where $n_x = 0$.

Due to the quadratic profile of the flow, the change in period $\Delta x(t)$ have opposite interpretation depending on if the particle is located in the upper or lower half of the channel. An increase of $\Delta x(t)$ means that the shear strength is decreasing. When a particle is located in the lower half of the channel this implies that the particle is drifting towards the center of the channel. If $\Delta x(t)$ decreases it means that the shear strength is increasing. Again, for a particle in the lower half of the channel, this implies that the particle is moving towards the bottom wall of the channel. The interpretation of which direction the particle is drifting due to the change in period $\Delta x(t)$ is the opposite if the particle is located on the upper half of the channel. The top panel of Figure 5.10 shows an example of how the period $\Delta x(t)$ for a particle changes as a function of time.

Under ideal conditions a particle is expected to move along a straight flowline since the flow is unidirectional. This is investigated by calculating the drift in the z-direction. The analysis program obtains the position of a particle and a line that represents the mean path is selected manually. This is shown in Figure 5.9. The drift in z is calculated as the deviation from this line.

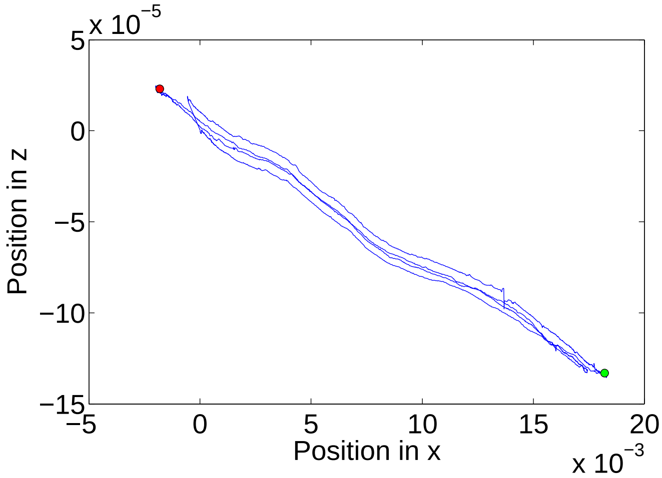

Figure 5.9: The figure shows the path of a particle during one measurement. The points on the blue lines denote the particles position in the channel. The slope of the line is caused by the fact that the channel is not perfectly aligned along the movable stage. The red and green dots are selected manually and the line between them is an approximation of the mean path of the particle. The drift Δz is calculated as the deviation from this line.

A drift in z might also affect the dynamics of a particle. Since the width of the channel is not infinite, there is a small shear s_z in the z-direction. Close to the edges, in the z-direction of the microchannel, the shear s_z becomes significant. At the beginning of a measurement, a particle is placed in the center of the channel with help of the optical tweezers. Here the shear strength s_z is zero, but for a particle that drifts too close to a channel wall the shear s_z will affect its orientational motion. The bottom panel in Figure 5.10 shows an example of the drift Δz of a particle during a measurement.

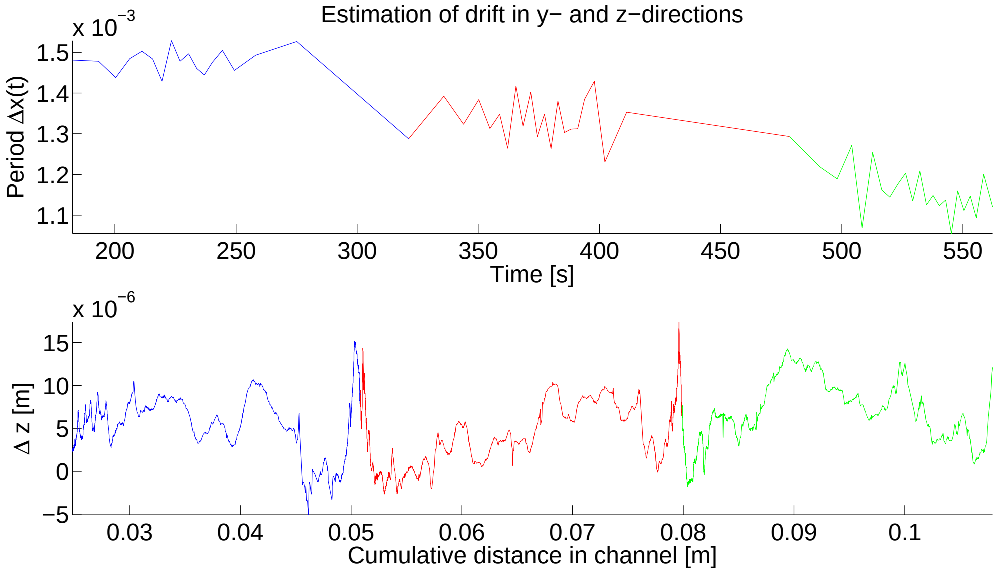

Figure 5.10: The figure shows the estimated drift in y and z. The top panel shows how the period $\Delta x(t)$ changes between flips and it is used to estimate the drift along the y-axis of the microchannel. The bottom panel shows the drift Δz, calculated as the deviation from the mean path of a particle.

5.2.5 Correction for diffraction effects

The cylindrical particles are made out of glass and they hence act as a lens. (This is what gives the particles a darker contrast). The observed length and width of a particle vary depending on the focus of the objective, which is illustrated with an example in Figure 5.11.

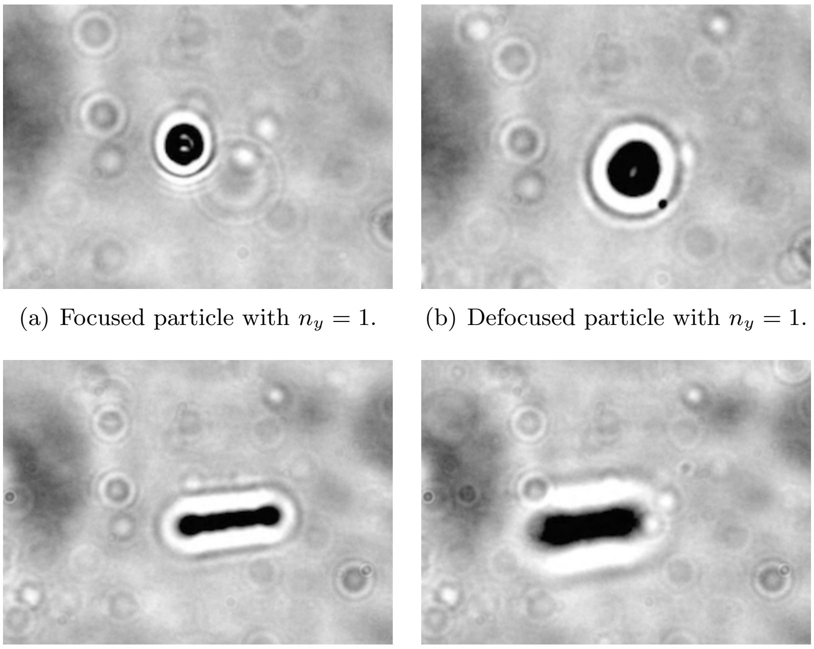

(a) Focused particle with $n_y = 1$. (b) Defocused particle with $n_y = 1$.

(c) Focused particle with $n_x = 1$. (d) Defocused particle with $n_x = 1$.

Figure 5.11: The figure illustrates how the interpreted length and width of a particle depends on the focus of the microscope objective. Panel a) and b) show a particle where $n_y = 1$. Hence, n_x and n_z are both supposed to be equal to zero. As seen in the images, even for the focused particle in panel a), an elliptic fit of the contour would have a length and width significantly greater than zero. As a consequence, at least one of the n_x and n_z components gets a value greater than zero. With the particle defocused, as in panel b), observed size of the contour increases. Panel c) and d) show the difference of the interpreted length and width for a particle where $n_x = 1$. In this case the focus of the microscope objective has less effect on the interpreted length, but it still has a significant effect of the interpreted width.

The problems from diffraction errors are most significant when a particle is close to $n_y = 1$. The projection of a particle lie in the x-z-plane and when $n_y = 1$, both the length and width of the projection should both be interpreted as zero. As seen in Figure 5.11 a) and b), where $n_y = 1$, it is easy to fit an ellipse to the projection with a width d and length l that are both significantly greater than zero.

A modification to the analysis program is made to reduce the problems from misinterpretations of the length and width of a particle when $n_y = 1$. When n_y equals one, the projection is very close to a circular disc, which means that $l = d$. By calculating the components of n_x and n_z as

$$\begin{aligned} n_x =& \frac{(l-d)\,\sin\alpha}{L_{\mathrm{rod}} - d}, \\ n_z =& \frac{(l-d)\,\cos\alpha}{L_{\mathrm{rod}} - d}, \end{aligned} \tag{5.2}$$

instead of as in Eqs. (5.1), n_x and n_z both equal to zero when l equals d. Since the width is also subtracted in the denominator, the orientation where $n_x = 1$ is still correctly recognized. The effect on the data due to this modification is shown in Figure 5.12.

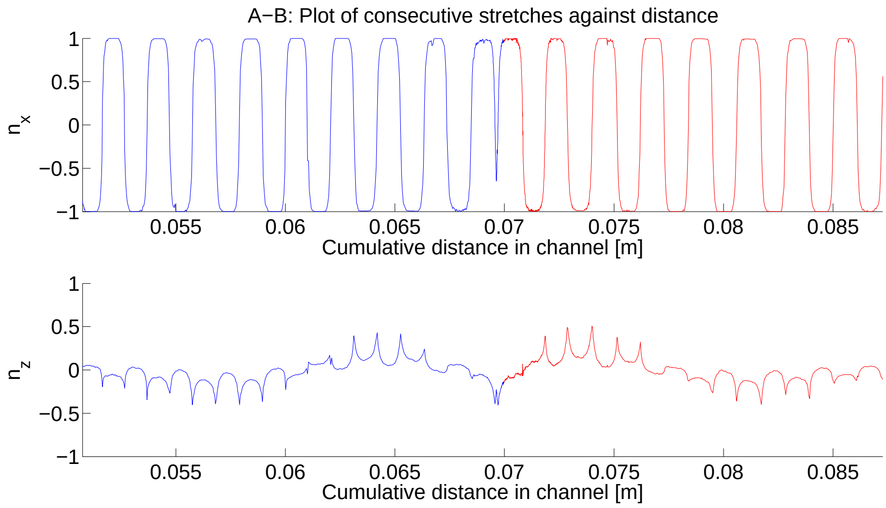

(a) Uncompensated data

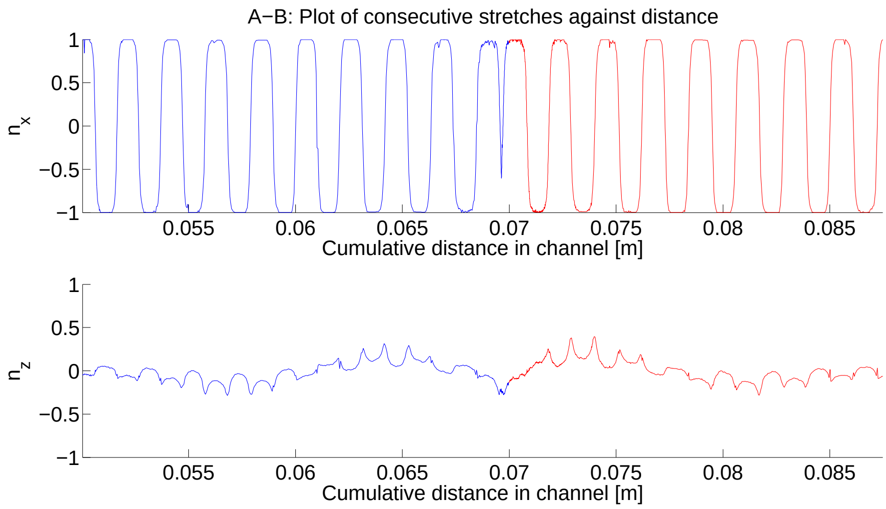

(b) Compensated data

Figure 5.12: The figure shows how the modifications to Eqs. (5.1) affect the amplitude of the n_z-peaks. The modification is shown in Eqs. (5.2). The effect is most significant for peaks close to $n_z = 0$, where the amplitude of the peaks is reduced. Panel a) shows the n_x and n_z components as calculated from Eq. (5.1). Panel b) shows the n_x and n_z components as calculated from Eq. (5.2).

5.2.6 Comparing the experimental data with Jeffery's equations

In this section a comparison between the experimental results and the equations of motion for an ellipsoidal particle is presented. As discussed in Section 4.3.2, the orientational dynamics of an ellipsoid is determined by the aspect ratio, asymmetry and initial conditions. Therefore, for the purpose of comparing the experimental data with Jeffery's equations, a database of simulated trajectories for ellipsoids with both varying aspect ratio λ_e, asymmetry ε and initial conditions is generated.

The aspect ratio λ_{rod} of a microrod can be determined with high accuracy since the diameter d_{rod} is well specified. Together with the rod length L_{rod}, obtained from the recordings, the aspect ratio for a rod is given by Eq. (4.9).

The asymmetry of a microrod is more difficult to determine and there is no known relation to the asymmetry of an ellipsoid. The best match for the asymmetry of a rod, for a given aspect ratio, is therefore found numerically by fitting the experimental data from each stretch of a microrod to the theoretical trajectories stored in the database. Not all the data on a stretch is included in the comparison. The included data is limited to the data points for n_z that corresponds to when n_x equals to zero, i.e. the data points that would be included in the Poincaré map. The best match between the experimental and theoretical data is selected with the least square method. An example of the result of matching the trajectory from a single stretch of a microrod to a theoretical trajectory of an ellipsoid is shown in Figure 5.13.

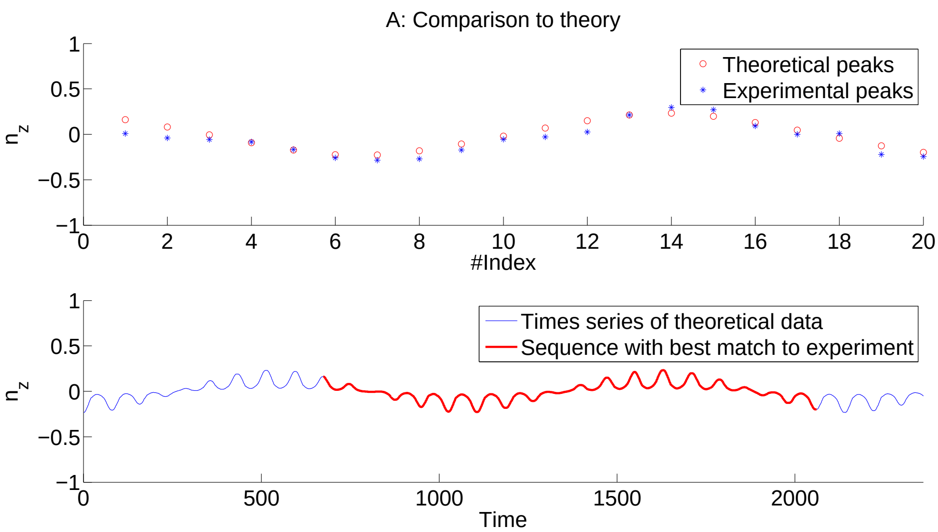

Figure 5.13: The top plot shows the fit of the n_z-peaks for a single stretch to the peaks of a theoretical time series. The peak values of n_z are taken as the values where $n_x = 0$. These are the values that correspond to the values on the vertical axis in a Poincaré map and the sequence of these points is unique for every orbit. The red section, in the bottom plot, is the theoretical time series that correspond the matched theoretical n_z-values.

The angle ψ for the experimental particles cannot be observed and the comparison is therefore only valid for the dynamics of θ and ϕ.

6

Results

THE results that are presented are a selection of the best data from the conducted experiments. During the process a lot of improvements have been made to the experimental setup and hence the latest data is the most relevant. In order to do a proper analysis of the data, it is also necessary that the prevailing conditions are the same for all measurements.

Data from three different particles are presented. The results for each particle are grouped into pairs of consecutive stretches, stretch A-B, C-D, etc. and each pair represent a different initial condition. For each pair, the data of the n_x and n_z-components are shown in a plot against the cumulative distance traveled in the microchannel, together with a plot of the same trajectories as function of position in the channel, the latter displays how well a particle retrace its trajectories before and after the reversing of the flow.

The comparison between the experimental data for each particle and theoretical trajectories of an ellipsoid, derived from Jeffery's equations is also presented for each particle. The comparison is presented in the Poincaré map of the matched ellipsoid, in which the position of the matched theoretical peaks is plotted.

The comparison is only valid for the $\mathbf{n}(t)$-components and does not take the dynamics of the angle ψ into account. The ψ-angle describes the rotation of a particle around its major semi-axis and it is not observable for the experimental microrods. Therefore, this parameter is not included in the comparison.

6.1 Particle 1

The experimental results for particle 1 contain 6 pairs of stretches. The particle has an aspect ratio of $\lambda_{\mathrm{rod}} = 6.6$ and it shows both periodic and quasi-periodic motions. The results for particle 1 are based on the same data as particle B in the work of Ankardal [2]. Figure 6.2 and 6.4 are based on the same data as Figure 5.6 in [2]. Figure 6.6 is based on the same data as Figure 5.7 and Figure 6.8 and 6.10 are based on the same data as Figure 5.8 in [2], respectively.

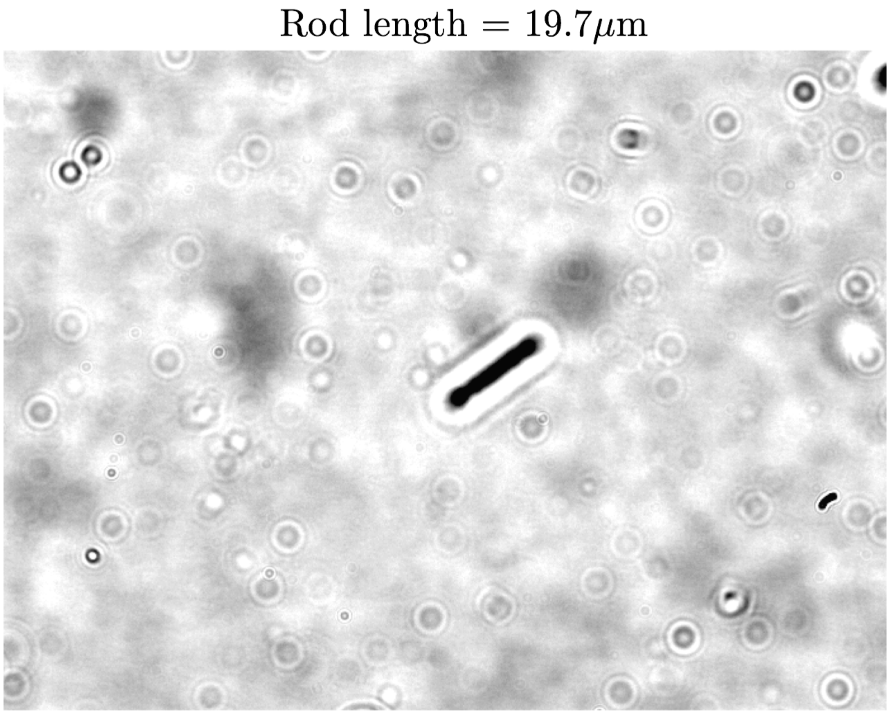

Figure 6.1: The estimated length of the particle is approximately 19.7μm. This gives the particle an aspect ratio of $\lambda_{\mathrm{rod}} = 6.6$.

6.1.1 Initial condition 1: Quasi-periodic motion

The data for n_z of particle 1 in stretches A-B show that the particle exhibits quasi-periodic motion where the amplitude of n_z varies but do not change sign. The trajectories, before and after the reversing of the flow, match in both phase and amplitude, shown in Figure 6.3.

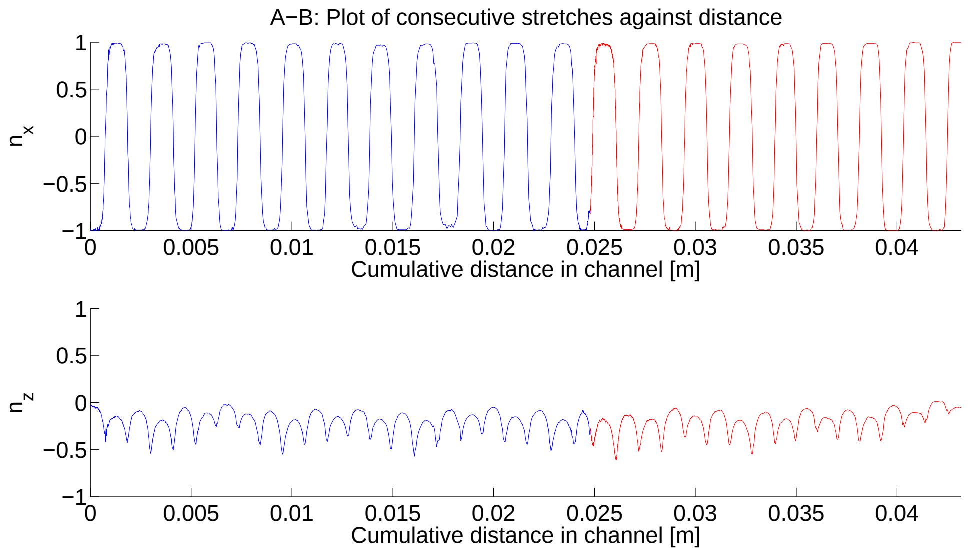

Figure 6.2: A plot of the amplitude of n_x and n_z. The amplitude of n_z varies but do not change sign. The variation in amplitude indicates quasi-periodic motion.

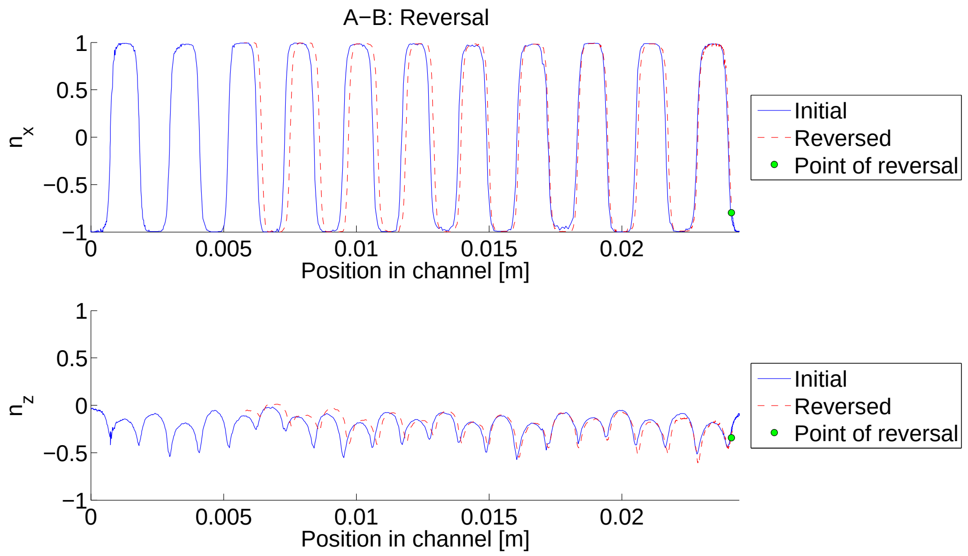

Figure 6.3: A plot of the trajectories from stretches A-B, at the reversing of the flow.

6.1.2 Initial condition 2: Quasi-periodic motion

The data for n_z of particle 1 in stretches C-D show that the particle exhibits quasi-periodic motion where the amplitude of n_z varies and changes sign. For the trajectories, before and after the reversing of the flow, there is a slight drift in both amplitude and phase, shown in Figure 6.5. The drift in phase is caused by density mismatch between the fluid and particle.

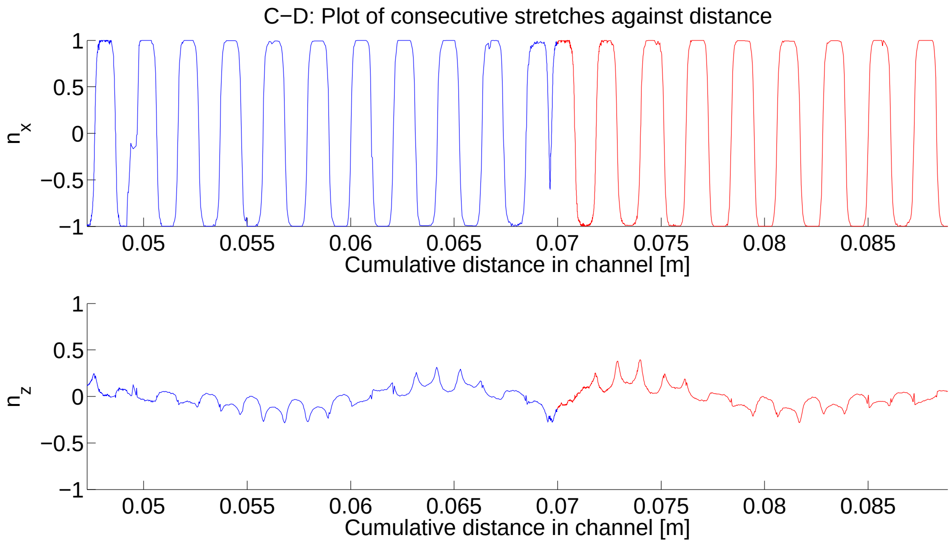

Figure 6.4: A plot of the amplitude of n_x and n_z. The amplitude of n_z varies and changes sign. The variation in amplitude indicates quasi-periodic motion.

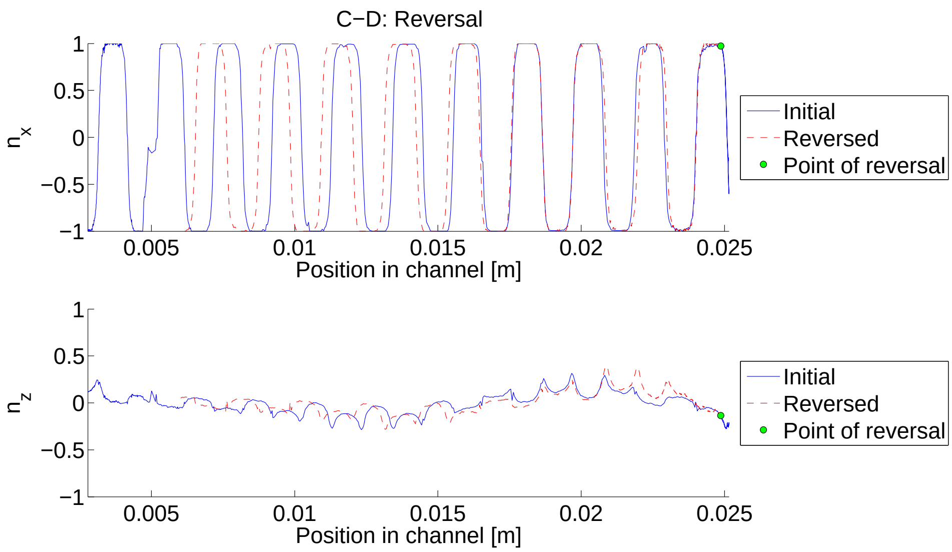

Figure 6.5: A plot of the trajectories from stretches C-D at the reversing of the flow.

6.1.3 Initial condition 3: Periodic motion

The data for n_z of particle 1 in stretches E-F show that the particle exhibits motion where the amplitude of n_z is constant. The motion resembles the dynamics of the periodic Jeffery orbits. The trajectories, before and after the reversing of the flow match well in both amplitude and phase, shown in Figure 6.7.

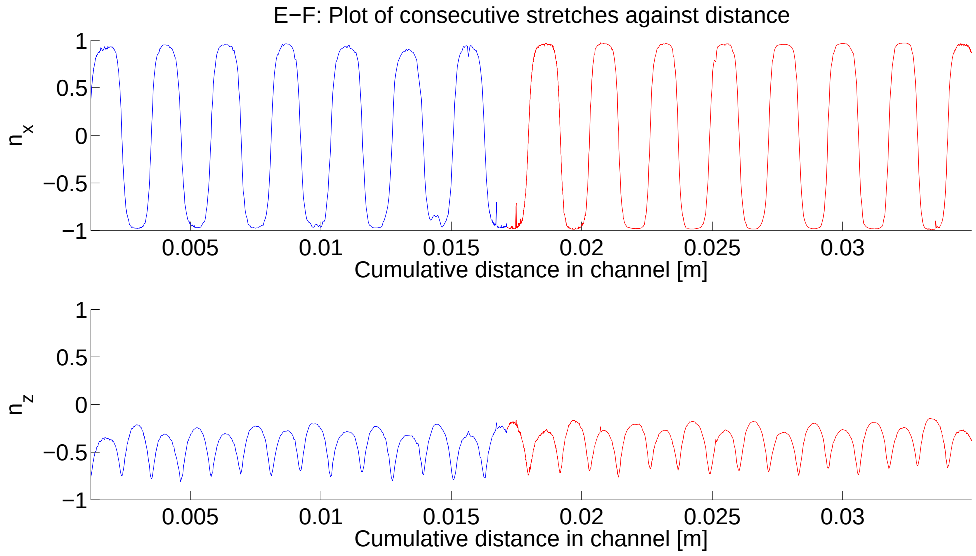

Figure 6.6: A plot of the amplitude of n_x and n_z. The n_z peaks keep constant amplitude, which resembles the dynamics of the Jeffery orbits.

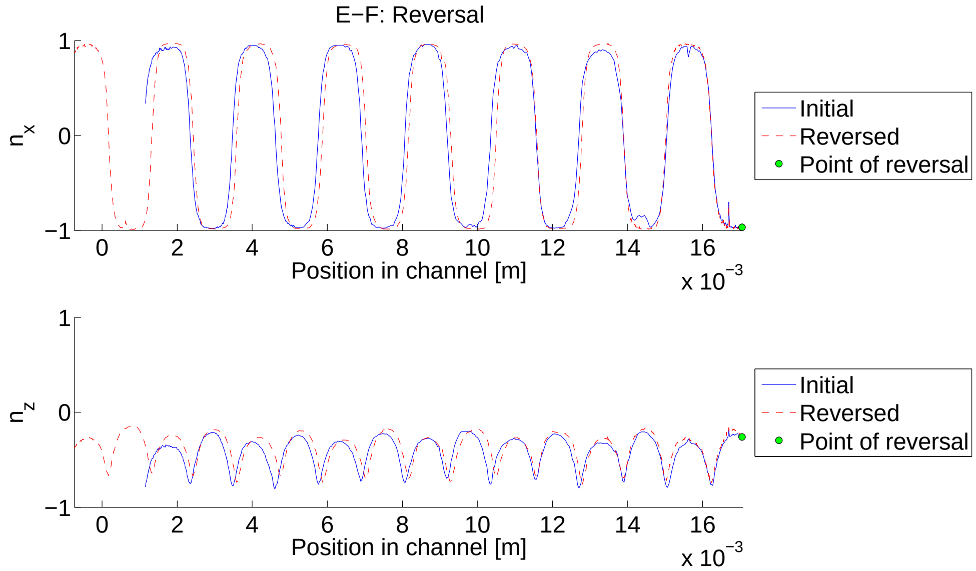

Figure 6.7: A plot of the trajectories from stretches E-F at the reversing of the flow.

6.1.4 Initial condition 4: Periodic motion

The data for n_z of particle 1 in stretches G-H show that the particle exhibits motion where the amplitude of n_z is constant and very close to one. The trajectories, before and after the reversing of the flow, match well in amplitude, shown in Figure 6.9. There is, however, a slight drift in phase due to mismatch in density between the fluid and particle.

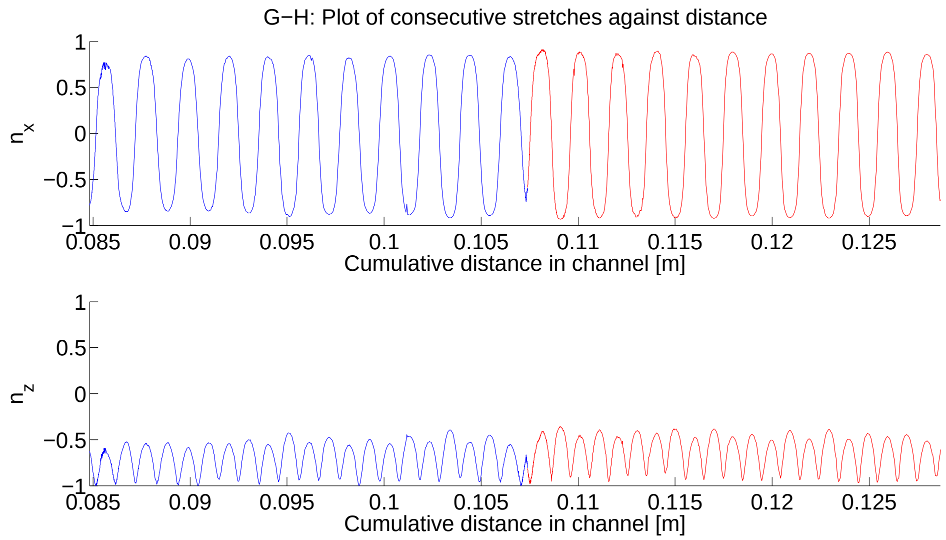

Figure 6.8: A plot of the amplitude of n_x and n_z. The n_z peaks keep constant amplitude, very close to $n_z = 1$.

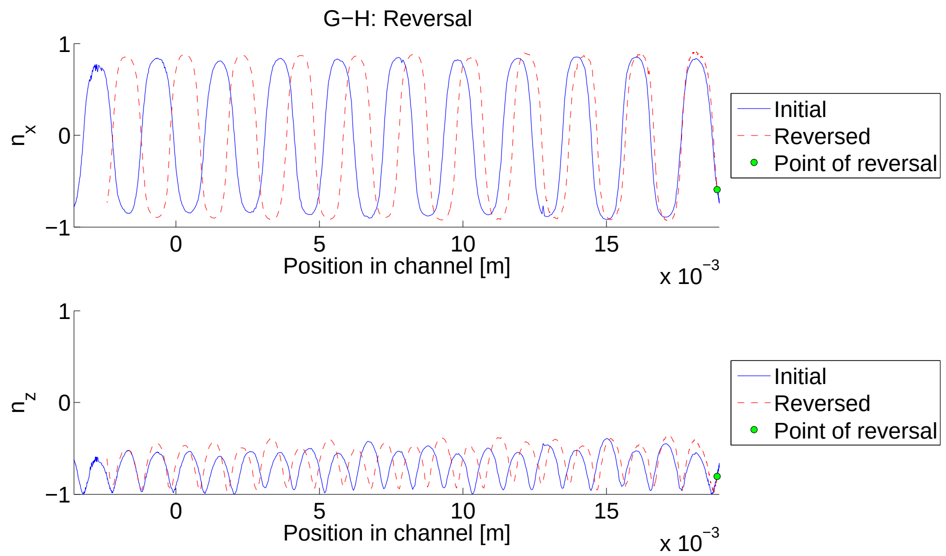

Figure 6.9: A plot of the trajectories from stretches G-H at the reversing of the flow.

6.1.5 Initial condition 5: Quasi-periodic motion

The data for n_z of particle 1 in stretches I-J show that the particle exhibits quasi-periodic motion where the amplitude of n_z varies and changes sign. The trajectories, before and after the reversal for the flow, match well in phase, shown in Figure 6.11. There is however, a slight drift in amplitude, which gets noticeable at the last part of stretch J.

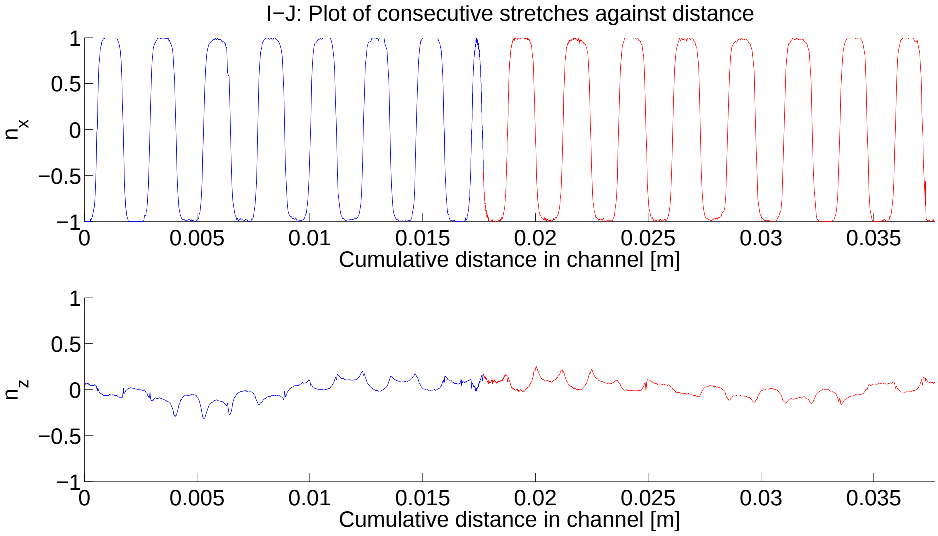

Figure 6.10: A plot of the amplitude of n_x and n_z. The amplitude of n_z varies and changes sign. The variation in amplitude indicates quasi-periodic motion.

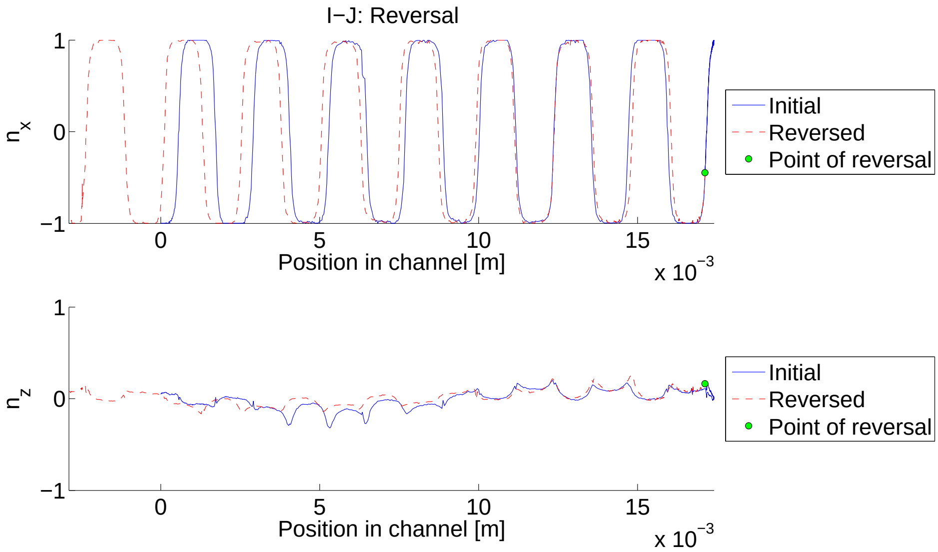

Figure 6.11: A plot of the trajectories from stretches I-J at the reversing of the flow.

6.1.6 Initial condition 6: Quasi-periodic motion

The data for n_z of particle 1 in stretches K-L show that the particle exhibits quasi-periodic motion where the amplitude of n_z changes sign. There is a slight drift in both amplitude and phase for the trajectories before and after the reversing of the flow, shown in Figure 6.13. The drift in phase is caused by mismatch in density between the fluid and particle.

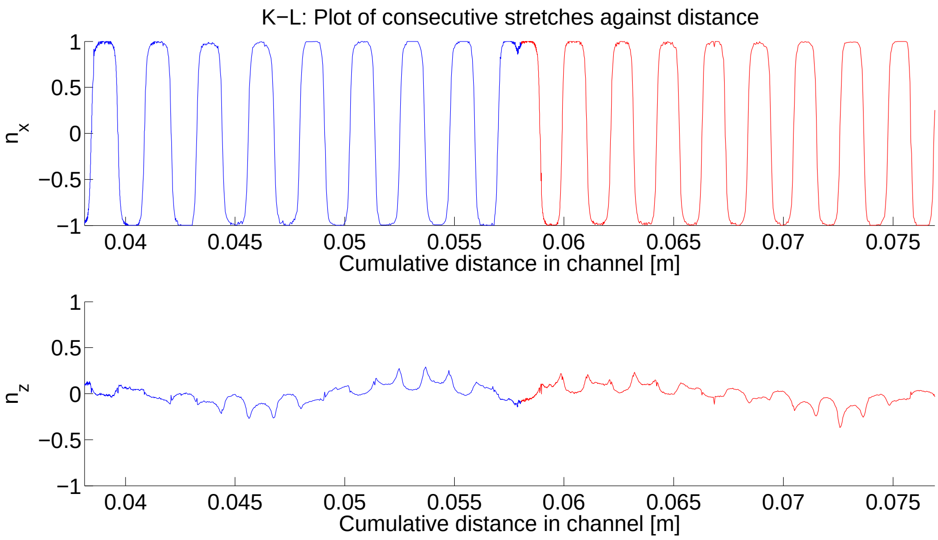

Figure 6.12: A plot of the amplitude of n_x and n_z. The amplitude of n_z varies in both amplitude and sign. The variation in amplitude indicates quasi-periodic motion.

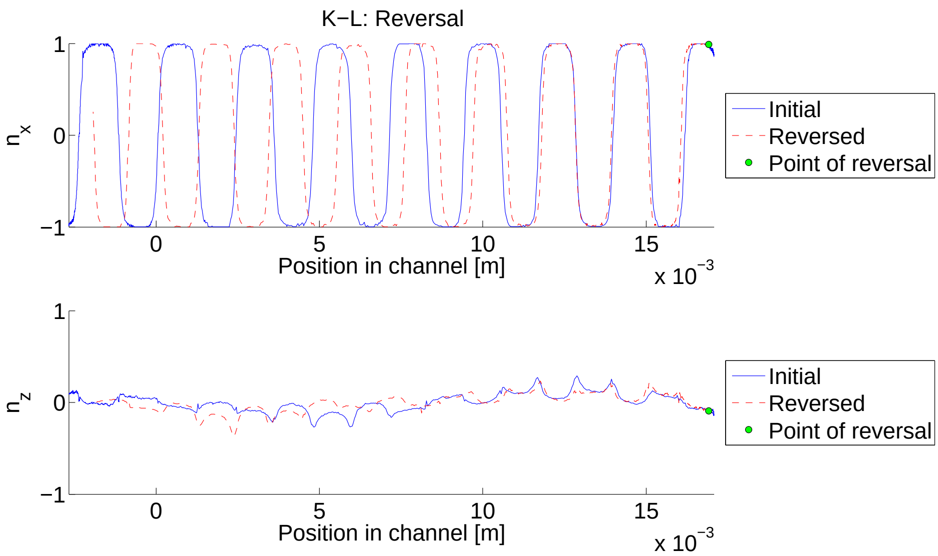

Figure 6.13: A plot of the trajectories from stretches K-L at the reversing of the flow.

6.1.7 Comparison to Jeffery's equations

Figure 6.14 shows the result of the comparison between the dynamics of particle 1 to the dynamics of an ellipsoid, derived from Jeffery's equations. The colored dots correspond to the position of the theoretical peaks that were matched to each stretch A-L of the experimental data.

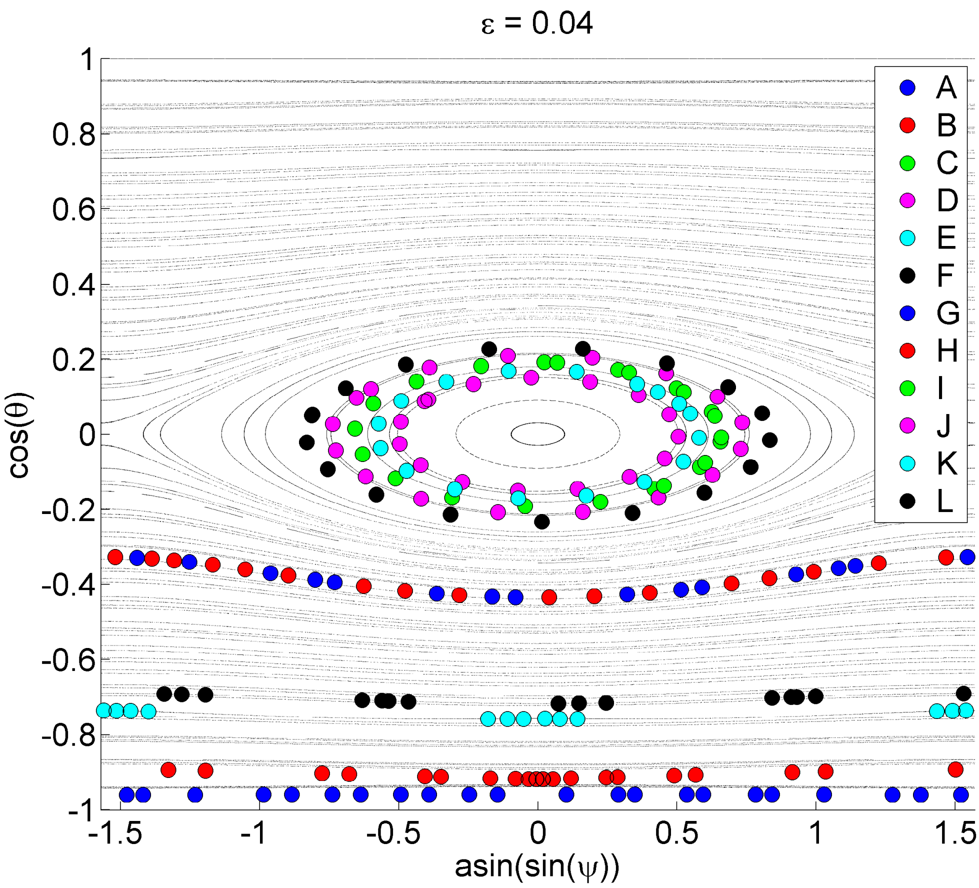

Figure 6.14: The figure shows a comparison between the data of particle 1 to the dynamics of an ellipsoid.

6.2 Particle 2

The experimental results for particle 2 contain 3 pairs of stretches. The particle has an aspect ratio of $\lambda_{\text{rod}} = 8.1$ and it shows both quasi-periodic and periodic motions. The results for particle 2 are based on the same data as particle A in the work of Ankardal [2]. Figure 6.18 is based on the same data as Figure 5.2 and Figure 6.20 is based on the same data as Figure 5.1 in Ankardal [2], respectively.

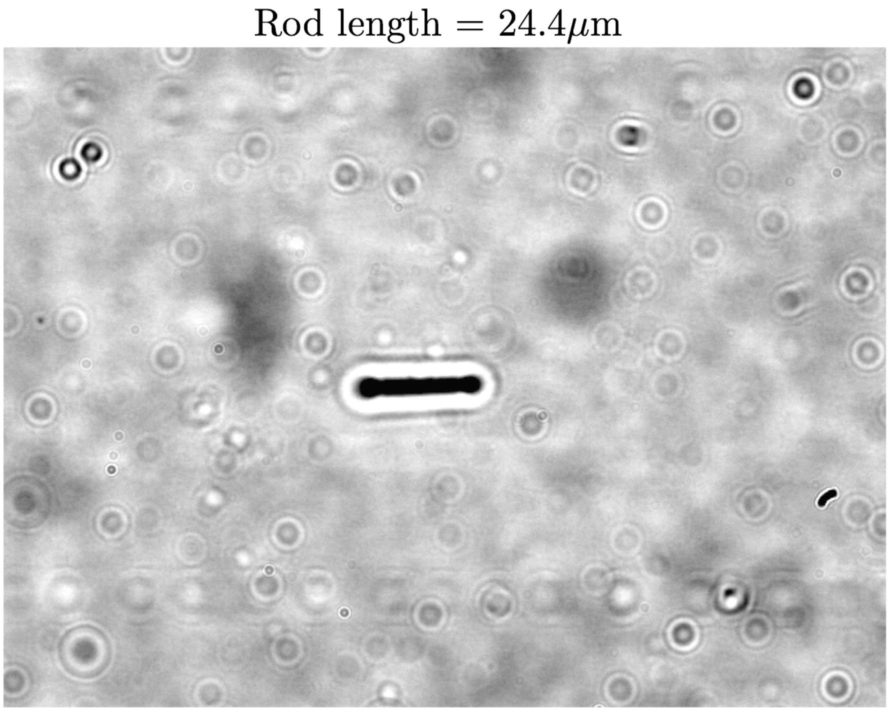

Figure 6.15: The estimated length of the particle is approximately 24.4μm. This gives the particle an aspect ratio of $\lambda_{\text{rod}} = 8.1$.

6.2.1 Initial condition 1: Periodic motion

The data for n_z of particle 2 in stretches A-B show that the particle exhibits motion where n_z keeps constant amplitude. The trajectories, before and after the reversing of the flow, match well in amplitude, while there is a slight drift in phase, shown in Figure 6.17. The drift in phase is caused by mismatch in density between the fluid and particle.

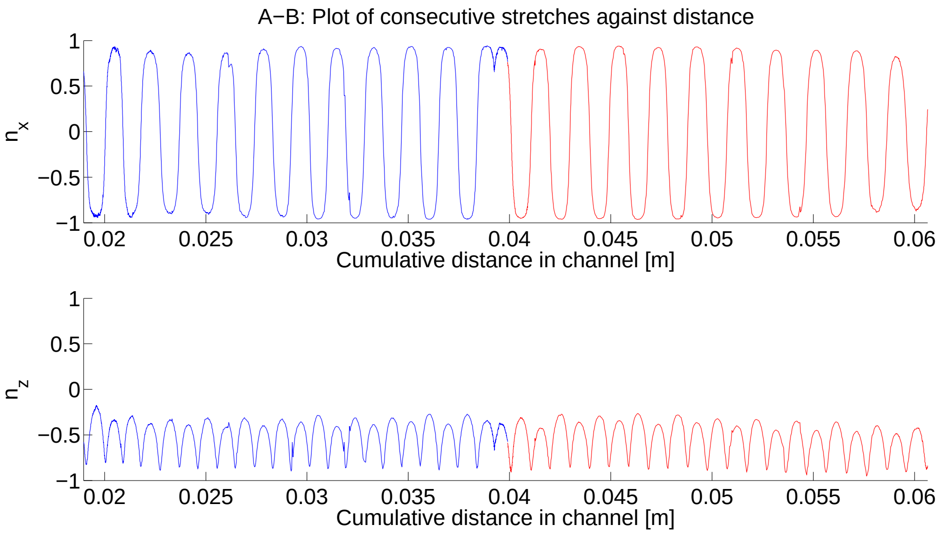

Figure 6.16: A plot of the amplitude of n_x and n_z. The n_z peaks keep constant amplitude, which indicates periodic motion.

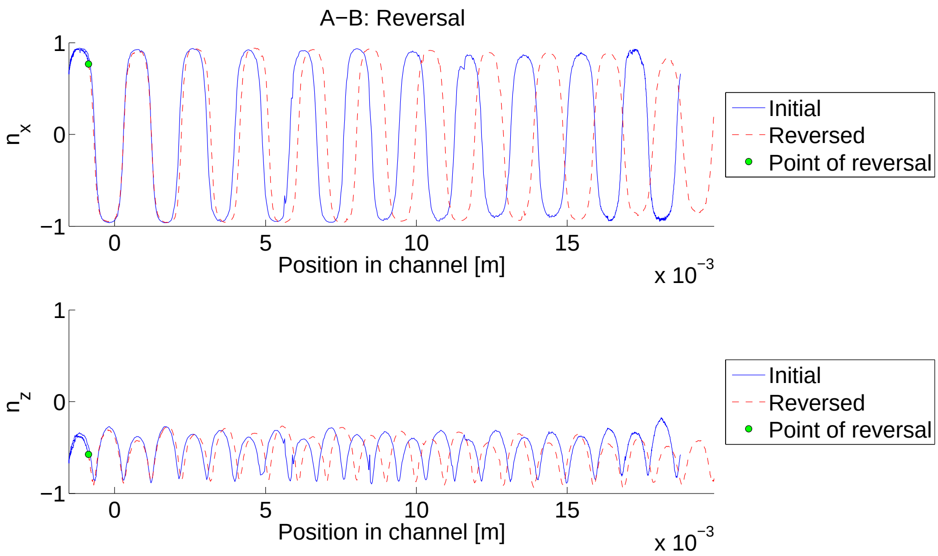

Figure 6.17: A plot of the trajectories from stretches A-B at the reversing of the flow.

6.2.2 Initial condition 2: Periodic motion

The data for n_z of particle 2 in stretches C-D show that the particle exhibits motion where n_z keeps constant amplitude. The trajectories, before and after the reversing of the flow, match well in amplitude but there is a slight drift in phase, shown in Figure 6.19. The drift in phase is caused by mismatch in density between the fluid and particle.

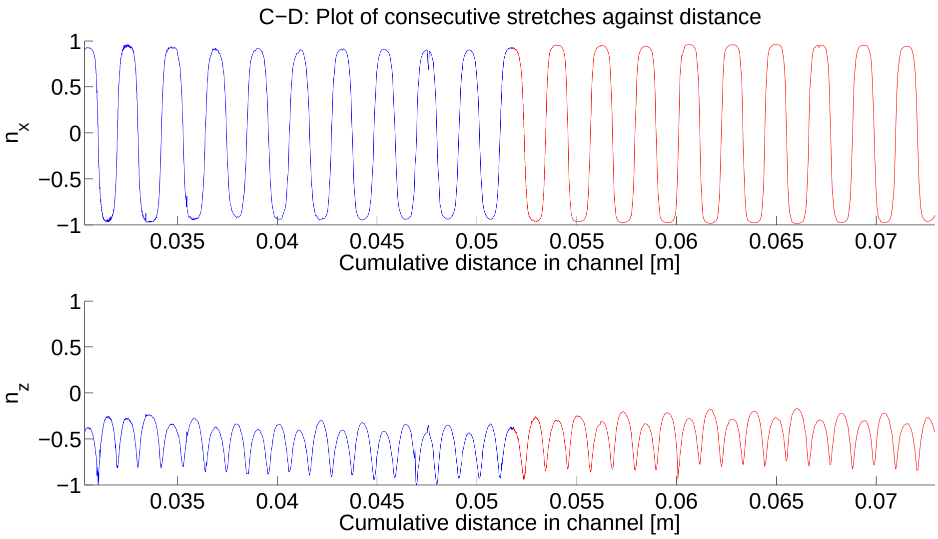

Figure 6.18: A plot of the amplitude of n_x and n_z. The n_z peaks keep constant amplitude, where n_z is close to one. The constant amplitude indicates periodic motion.

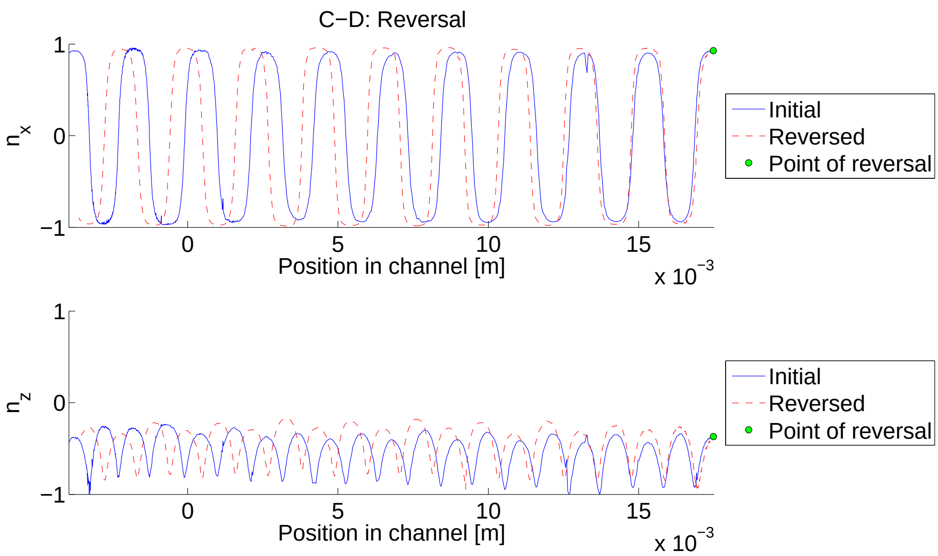

Figure 6.19: A plot of the trajectories from stretches C-D at the reversing of the flow.

6.2.3 Initial condition 3: Quasi-periodic motion

The data for n_z of particle 2 in stretches E-F show that the particle exhibits motion where the amplitude of n_z is close to constant at $n_z = 0$. There is, however, a slight quasi-periodic behavior for stretch E where n_z changes sign. The trajectories before and after the reversing of the flow match well in phase, shown in Figure 6.21.

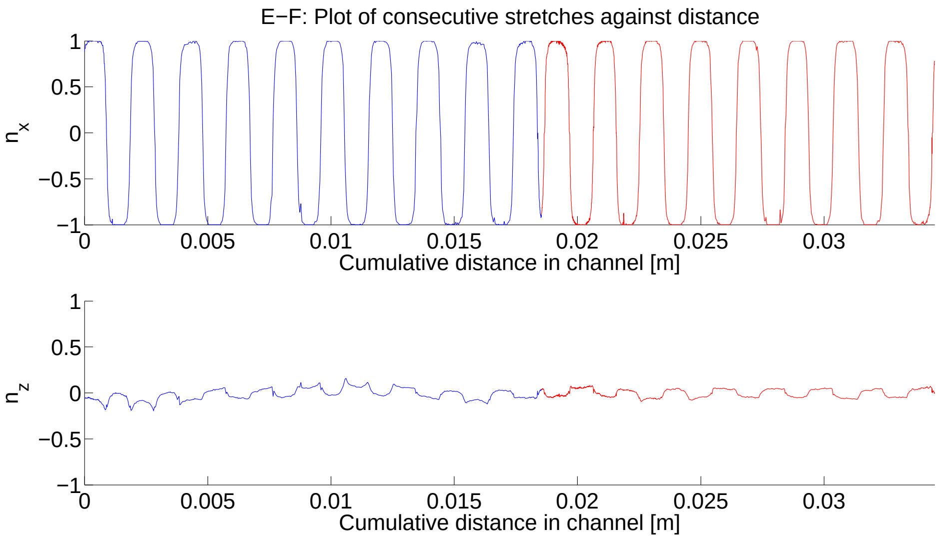

Figure 6.20: A plot of the amplitude of n_x and n_z. For stretch E the amplitude of n_z shows slight quasi-periodic motion, where the amplitude changes sign. The amplitude of n_z in stretch F stays close to constant at zero.

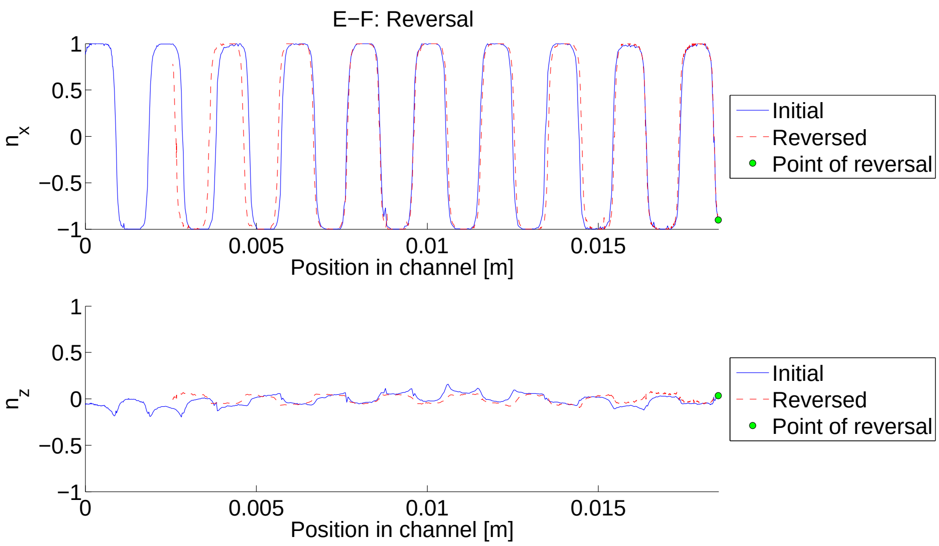

Figure 6.21: A plot of trajectories from stretches E-F at the reversing of the flow.

6.2.4 Comparison to Jeffery's equations

Figure 6.22 shows the result of the comparison between the motion dynamics of particle 2 to the motion dynamics of an ellipsoid, derived from Jeffery's equations. The colored dots correspond to the position of the theoretical peaks that were matched to each stretch of the experimental data.

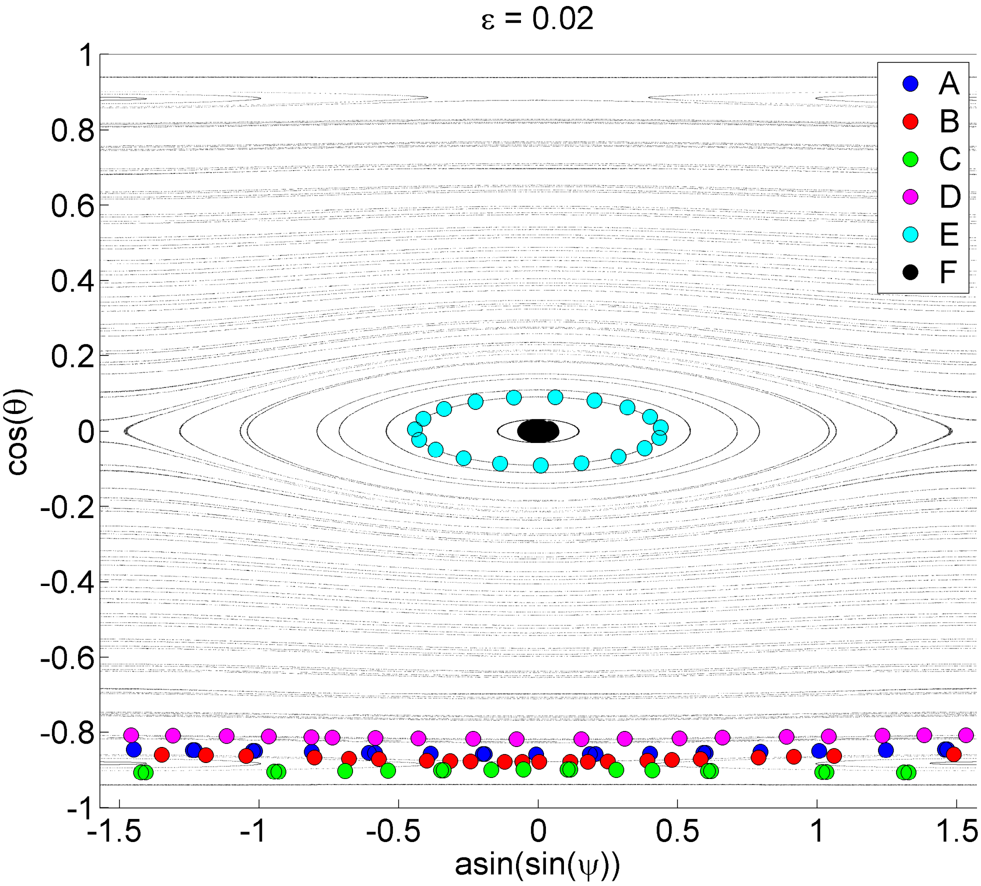

Figure 6.22: The figure shows a comparison between the experimental data of particle 2 to the dynamics of an ellipsoid. The peaks in stretch E is matched to a trajectory with higher amplitude than the peaks in stretch F due to the slight quasi-periodic motion.

6.3 Particle 3

The experimental results for particle 3 contain 2 pairs of stretches. It has an aspect ratio of $\lambda_{\text{rod}} = 6.9$. The particle is included because it shows the two different types of quasi-periodic motion on the same stretch. This is not in accordance with Jeffery's theories, unless it is a chaotic trajectory. The database of theoretical trajectories contains very few chaotic ones and it was therefore not possible to find a good match to the experimental data of particle 3.

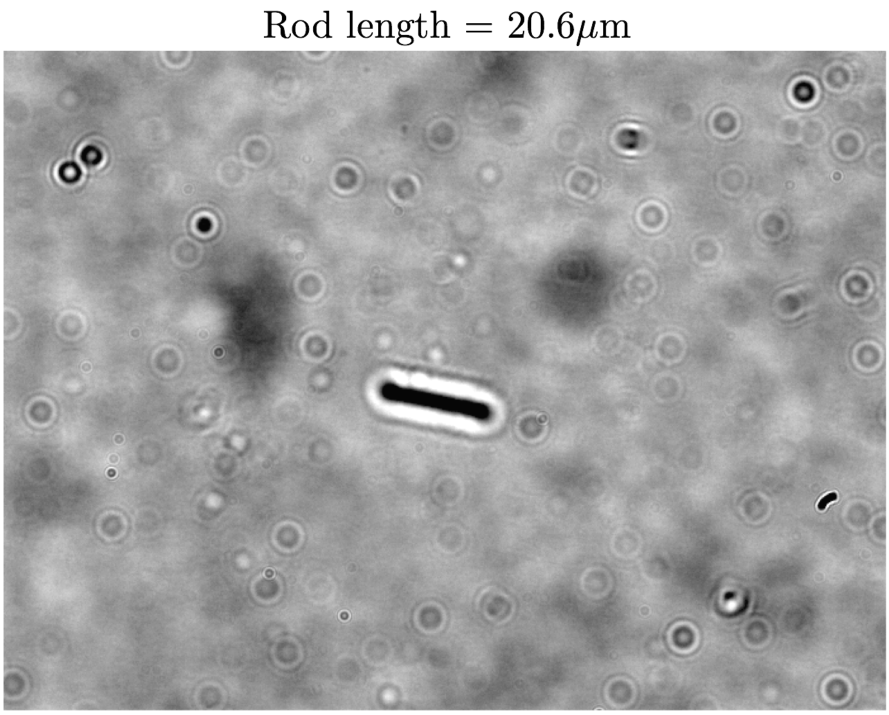

Figure 6.23: The estimated length of the particle is approximately 20.6μm. This gives the particle an aspect ratio of $\lambda_{\text{rod}} = 6.9$.

6.3.1 Initial condition 1: Periodic motion

The data for n_z of particle 3 in stretches A-B show that the particle exhibits motion where n_z keeps constant amplitude. The trajectories, before and after the reversing of the flow, match well in amplitude, while there is a slight drift in phase, shown in Figure 6.25. The drift in phase is caused by mismatch in density between the fluid and particles.

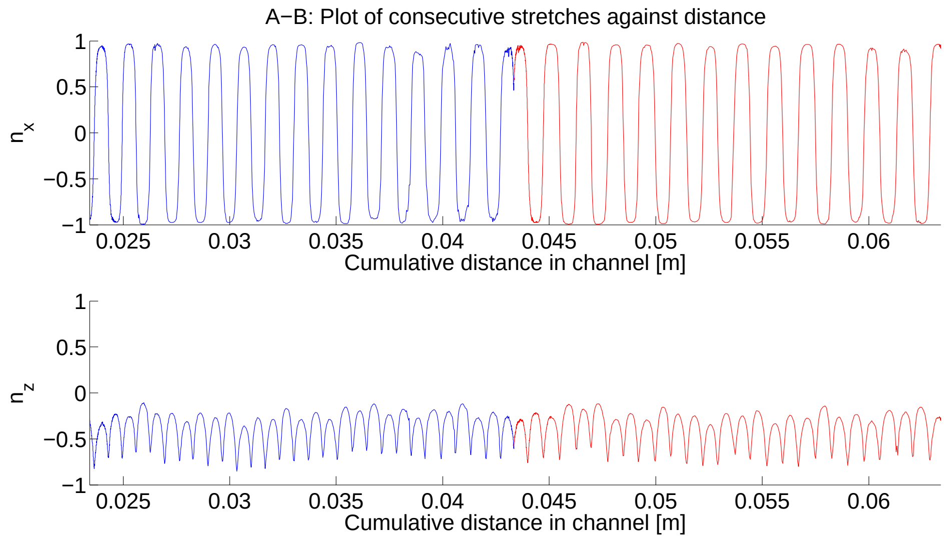

Figure 6.24: A plot of the amplitude of n_x and n_z. The n_z peaks keep constant amplitude, which indicates periodic motion.

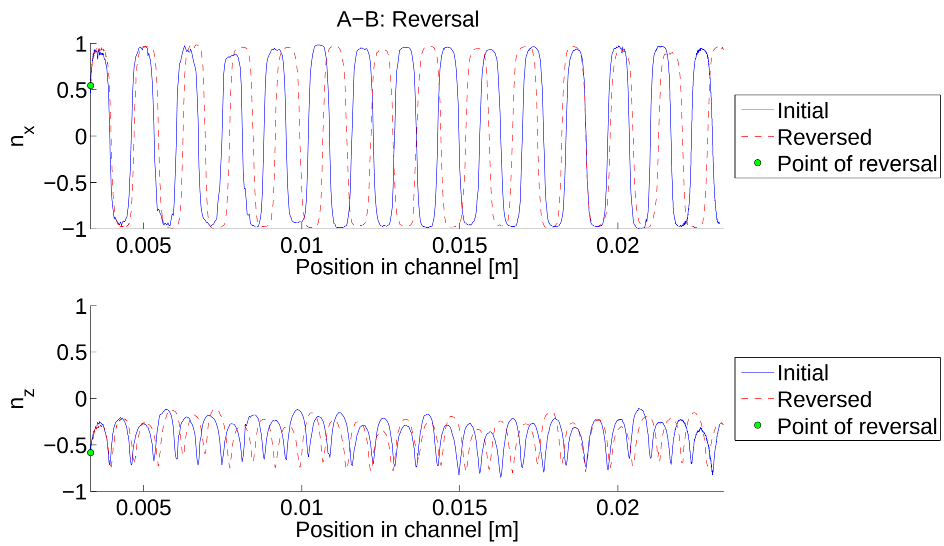

Figure 6.25: A plot of the trajectories from stretches A-B at the reversing of the flow.

6.3.2 Initial condition 2

The data for n_z of particle 3 in stretches C-D show that the particle exhibits chaotic motion. The trajectory of a single stretch shows features of quasi-periodic motion, where n_z both changes sign and where it does not. The trajectories before and after the reversal match well in phase, while there is a small mismatch in amplitude.

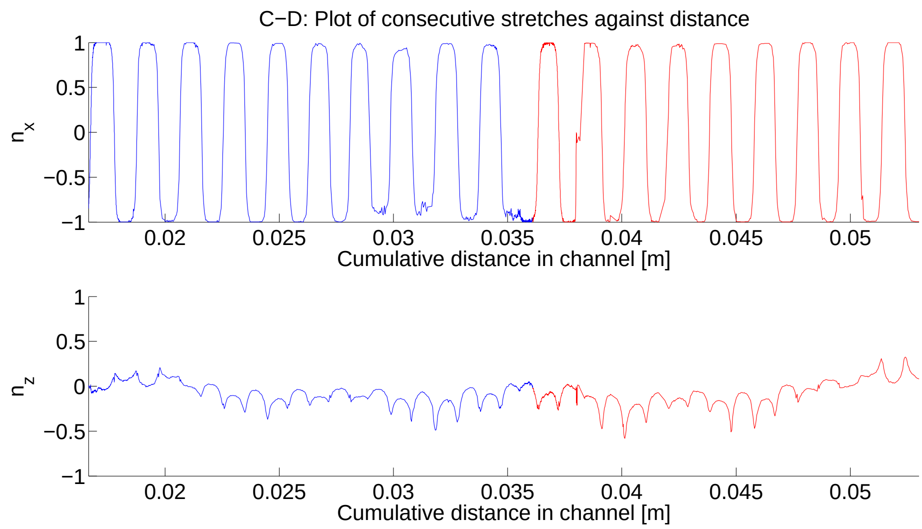

Figure 6.26: A plot of the amplitude of n_x and n_z. The last part of stretch C and first part of stretch D show quasi-periodic motion where the amplitude of the n_z-peaks varies without changing sign. The first part of stretch C and last part of stretch D show quasi-periodic motion where n_z changes sign.

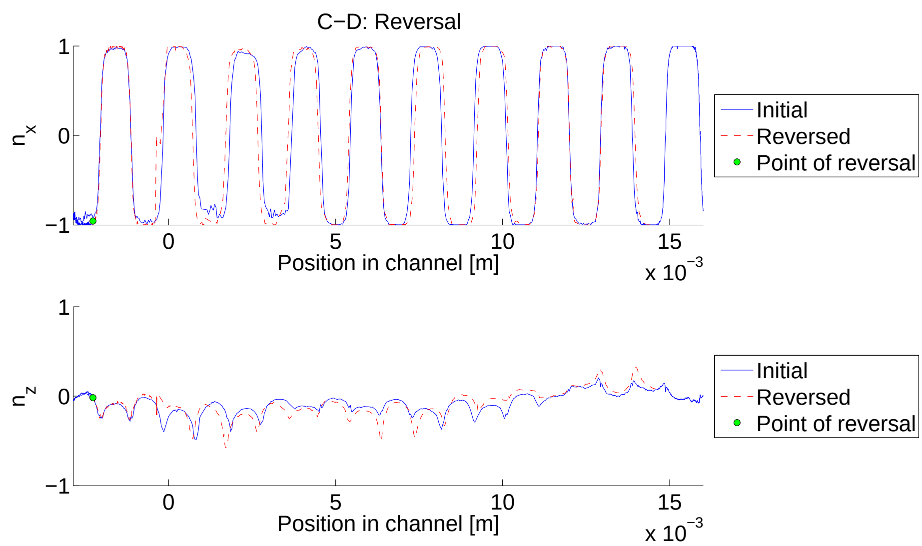

Figure 6.27: A plot of the trajectories from stretches C-D at the reversing of the flow.

6.3.3 Comparison to Jeffery's equations

Figure 6.28 shows the result of the comparison between the motion dynamics of particle 3 to the motion dynamics of an ellipsoid, derived from Jeffery's equations. The colored dots correspond to the position of the theoretical peaks that were matched to each stretch of the experimental data.

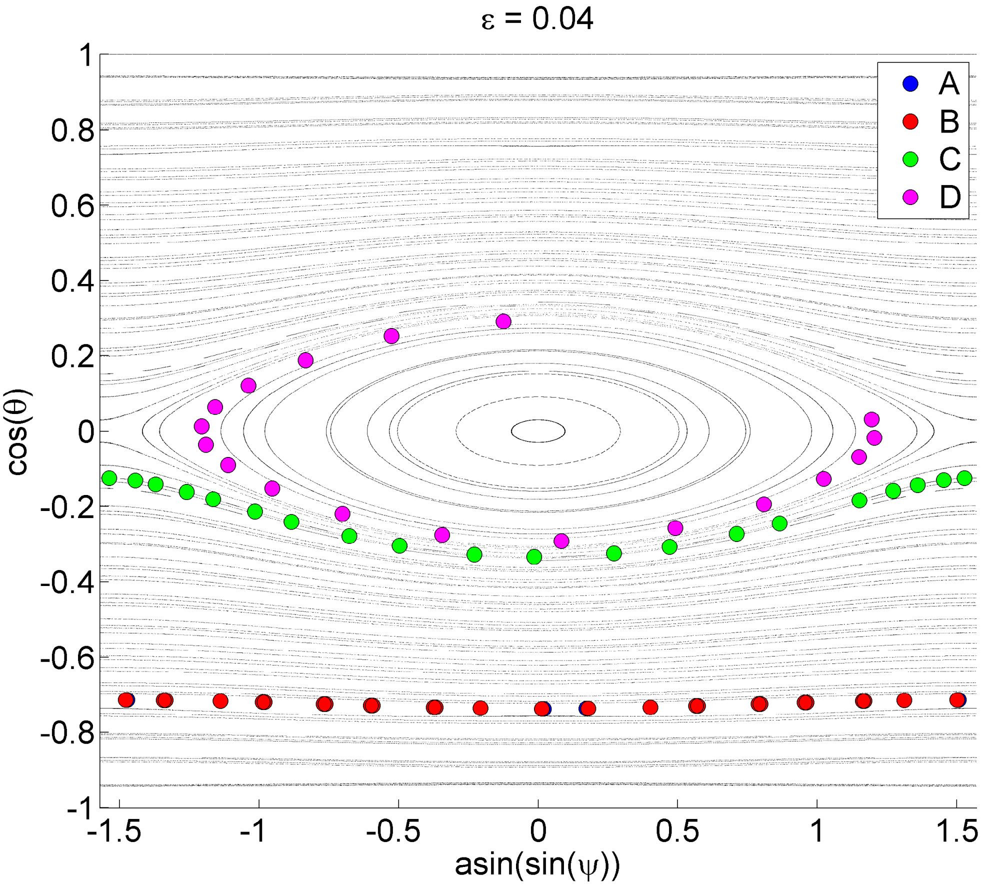

Figure 6.28: The figure shows a comparison between the experimental data of particle 3 to the dynamics of an ellipsoid. The lack of chaotic trajectories in the database results in a poor match between the experimental data and the theoretical trajectories.

7

Discussion

The success rate of obtaining measurements where a particle successfully retraces its trajectory after reversing the flow has increased progressively during the work of this thesis. But improvements that increase the success rate of retraced trajectories even further, or at least narrow down the possible factors for non-retracing trajectories after a reversal are of interest.

The results section shows measurements for three different particles where the trajectories of the particles were successfully retraced after the reversing of the flow, for more than one initial condition. In this section a discussion on the quality of the experimental results, possible improvements to the experiment and outlook for future experiments is presented.

7.1 Steadiness of the flow

One obvious improvement to the experiments is to increase the stability of the velocity of the flow. When changing the direction of the flow, there is a substantial delay until the velocity of a particle reaches its steady maximum, as seen in Figure 7.1.

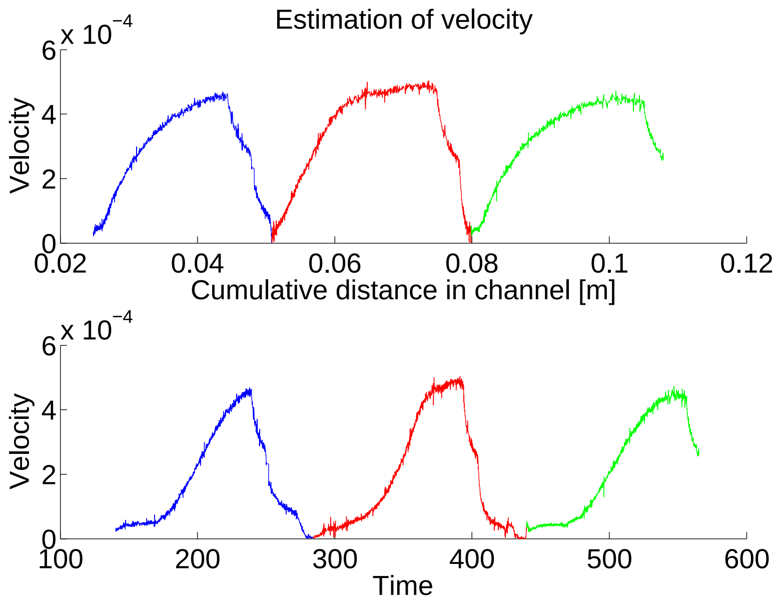

Figure 7.1: The plot shows the magnitude of the velocity of a particle in the x-direction of the channel. A slow deceleration and acceleration at the reversal is observed for all measurements. The velocity accelerates over an entire stretch without reaching its steady maximum. With an incompressible fluid and with both the fluid and the particles close to inertialess, the particles are expected to reach a steady velocity much faster. In the first reversal in this figure the pump changes from withdrawal to infusion and the second one shows the opposite.

The velocity of a particle is approximately equal to the velocity of the flow. Figure 7.1 shows the absolute value of the velocity and the first two steps of the reversal can easily be distinguished. However, there is a deceleration and acceleration of the flow velocity between the steps. The fluid is incompressible and both the fluid and particles are close to inertialess. The change in flow velocity between the steps should then be instantaneous. A likely explanation to the slow change in velocity is flexibility in the channel, tubing or syringe or a combination of the three.

The direction of the flow is controlled by adjusting the pressure gradient in the fluid, since increasing or decreasing the volume amount of fluid in the syringe is equivalent to an increase or decrease of the pressure applied by the syringe. If the channel, tubing and syringe had zero flexibility, the only path for the fluid when the pressure changes, is through the outlet of the channel, i.e. in the x-direction. The change in flow velocity would then be instantaneous. Since the flow accelerates slowly, even when the pump is running at maximum speed, this suggests that the pressure-change provided by the pump after the reversing of the flow, expand or contract the system (depending on if the pump is running at infusion or withdrawal after the reversal) rather than pushing the fluid through the channel. Hence, making the mentioned components stiffer could reduce the delayed change in velocity. A second way to minimize possible expansion effects is to make the radius of the inlets larger, making it easier for the fluid to enter or escape the channel.

Having a more stable flow minimizes the risk of pressure fluctuations to be the cause of the unsuccessful retracing of trajectories during the reversing of the flow.

7.2 Quality of the results

In the work of [12, 24, 30] both periodic and quasi-periodic of motion of polymer rods were observed. Unfortunately they did not observe different behaviors for the same particle. The purpose of this thesis was to investigate the dependence of the initial conditions for a microrod for its orientational dynamics.

The results shows measurements for three different particles where the trajectories of the particles were successfully retraced after the reversing of the flow, for more than one initial condition. The trajectories of the microrods show a lot of similarities to the motion of ellipsoidal particles. For almost all measurements, where the particles successfully retrace their trajectory, the trajectories resemble either the periodic or quasi-periodic motion that are found for ellipsoidal particles with similar initial conditions. But once again, this comparison is only valid for the time series of the orientation vector $\mathbf{n}(t)$, which only contain information about the θ and ϕ-angle. The results do not contain information about the angle ψ that describes the rotation around the major axis of a rod.

The variety of initial conditions is important to limit the number of possible data matches in the comparison with ellipsoids. For most asymmetries ε of an ellipsoid, $\cos\theta$ is a constant of motion for trajectories at the edges of the Poincaré map. Observing such a trajectory therefore provide minimal information about the features of the rest of the particle's Poincaré map. The trajectories that best limit the number of matching ellipsoids are found in the center of the Poincaré map. This means that, in order to verify how well Jeffery's equations describe the orientational motion of the microrods, a variety of different trajectories for each particle is needed.

Particle 1 stands out when it comes to both quality and quantity of the successful measurements. This is merely a coincidence. Data from a number of particles with 2-3 successful reversals have been collected. However, the observed trajectories for these particles do not have enough variety of initial conditions that they are worth presenting.

7.3 Outlook

The outlook for future experiments is promising. With the optical tweezers in place, a possible continuation of this work is to measure the dynamics of other particle shapes, such as crosses. The geometry of crosses makes it possible to observe all rotational degrees of freedom. However, more results for microrods need to be obtained in order to verify if their orientational motion can be described by Jeffery's equations.

There are two important theoretical questions that need to be answered in order to understand how well Jeffery's equations can describe the orientational motion of deformed cylinders. First, Jeffery's equations describe the orientational motion of a particle in a linear shear flow. In the experiments the linear shear flow is approximated by a Poiseuille flow, where the curvature of the flow is assumed to be negligible due to the small dimensions of the particles. Chwang [10], Ingber and Mondy [22] showed that Jeffery's equations are valid for a Poiseuille flow in the case for axisymmetric particles but it has not been verified for the case of non-axisymmetric particles. Second, the cylindrical particles are usually deformed in a way that they do not possess any axes of symmetry. An ellipsoidal particle has three axes of symmetry. It is necessary to understand how the absence of symmetry-axes affects the equations of motion. The experimental results suggest that in the case of deformed cylinders, if the angle ψ is neglected, the motion closely resemble the motion of ellipsoids. It is, however, possible that the dynamics of the ψ-angle differs a lot from that described by Jeffery's equations, which means that the equations for θ and ψ also are different.

8

Summary

THE orientational motion of cylindrical microrods, immersed in a creeping shear flow through a microchannel, has been investigated by analyzing the times series of the orientation-vector $\mathbf{n}(t)$ for the major axis of a rod as the rod rotates in the flow. The experiment is a continuation of the work initiated by Einarsson *et al.* [12] and the work has included improvements to the experimental setup. The polymer fibers that were used in the previous epxeriments were replaced by more regularly shaped glass microrods. The microrods have a well-defined diameter, which made it easier to determine their aspect ratio λ_{rod}. However, the asymmetry of the microrods derives from irregularities on the rod ends, which made it difficult to determine.

A fluid composed by water, glycerol and sodium metatungstate monohydrate has been used to match the density of the glass microrods. The new fluid is less viscous than glycerol, which was previously used, making it more responsive to pressure fluctuations.

Optical tweezers were installed for the purpose of changing the orientational initial conditions for a single particle. The tweezers made it possible to investigate how the choice of initial orientation affects the dynamics of a particle. The results show that by controlling the initial conditions, it was possible to observe either quasi-periodic or periodic motion for a particle. The results show a lot of similarities with Jeffery's equations of motion (4.11), for an arbitrary ellipsoid. Microrods with initial conditions close to perpendicular to both the flow and shear direction were more likely to show periodic motion, while particles with initial conditions close to aligned with the shear direction and perpendicular to the flow were more likely to show quasi-periodic motion.

Analysis of the trajectory of a particle before and after the reversing of the flow was performed to find out if the particles experience any inertial effects. If a particle successfully retraces its trajectory after the reversing of the flow, the absence of inertial effects for the particle is guaranteed. Particles with orientational initial conditions such that they are close to perpendicular to both the flow and shear direction had a higher success rate of retracing their trajectories after the reversing of the flow.

A comparison of the experimental results to trajectories derived from Jeffery's equations of motion of ellipsoidal particles with a ranging aspect ratio and asymmetry was also made. With high number of measurements, from a variety of initial conditions, the number of possible matching ellipsoids was narrowed down. However, the comparison is only valid for the normal components $\mathbf{n}(t)$. The data do not contain any information about the rotational angle around the major semi-axis of a rod.

Bibliography

[1] Almog, Y. and Frankel, I. [1995], 'Motion of axisymmetric dipolar particles in homogeneous shear flow', *Journal of Fluid Mechanics* **289**, 243–261.

[2] Ankardal, S. [2014], Experimental measurements of the Jeffery orbits of microrods in a microchannel. M.Sc. Thesis, Chalmers University of Technology.

[3] Ashkin, A. [1992], 'Forces of a single-beam gradient laser trap on a dielectric sphere in the ray optics regime', *Biophysical Journal* **61**(2), 569–582.

[4] Bareil, P. B. and Sheng, Y. [2010], 'Angular and position stability of a nanorod trapped in an optical tweezers', *Opt. Express* **18**(25), 26388–26398.
URL: *http://www.opticsexpress.org/abstract.cfm?URI=oe-18-25-26388*

[5] Bonessi, D., Bonin, K. and Walker, T. [2007], 'Optical forces on particles of arbitrary shape and size', *Journal of Optics A: Pure and Applied Optics* **9**(8), S228.
URL: *http://stacks.iop.org/1464-4258/9/i=8/a=S16*

[6] Brenner, H. and Bungay, P. M. [1971], 'Rigid-particle and liquid-droplet models of red cell motion in capillary tubes.', *Fed Proc* **30**(5), 1565–77.

[7] Bretherton, F. P. [1962], 'The motion of rigid particles in a shear flow at low Reynolds number', *Journal of Fluid Mechanics* **14**, 284–304.

[8] *Cell Spacing for LCDs (Microrods)* [n.d.].
URL: *http://www.neg.co.jp/EN/product/LCD.html*

[9] Chen, J.-P. and Lamb, D. [1994], 'The theoretical basis for the parameterization of ice crystal habits: Growth by vapor deposition', *Journal of the Atmospheric Sciences* **51**(9), 1206–1222.

[10] Chwang, A. T. [1975], 'Hydromechanics of low-Reynolds-number flow. Part 3. Motion of a spheroidal particle in quadratic flows', *Journal of Fluid Mechanics* **72**, 17–34.
URL: *http://journals.cambridge.org/article_S0022112075002911*

[11] Davis, R. H. [1991], 'Sedimentation of axisymmetric particles in shear flows', *Physics of Fluids A: Fluid Dynamics (1989-1993)* **3**(9), 2051–2060.

[12] Einarsson, J., Johansson, A., Mahato, S., Mishra, Y., Angilella, J., Hanstorp, D. and Mehlig, B. [2013], 'Periodic and aperiodic tumbling of microrods advected in a microchannel flow', *Acta Mechanica* **224**(10), 2281–2289.
URL: *http://dx.doi.org/10.1007/s00707-013-0924-0*

[13] Galvin, K. P. and Nguyentranlam, G. [2002], 'Influence of parallel inclined plates in a liquid fluidized bed system', *Chemical Engineering Science* **57**, 1231–1234.

[14] Gauthier, R. [1997], 'Theoretical investigation of the optical trapping force and torque on cylindrical micro-objects', *Journal of the Optical Society of America B* **14**(12), 3323– 3333.

[15] Glazier, J. and Libchaber, A. [1988], 'Quasi-periodicity and dynamical systems: An experimentalist's view', *Circuits and Systems, IEEE Transactions on* **35**(7), 790–809.

[16] Goldsmith, H. and Mason, S. [1962], 'The flow of suspensions through tubes. I. Single spheres, rods, and discs', *Journal of Colloid Science* **17**(5), 448 – 476.
URL: *http://www.sciencedirect.com/science/article/pii/0095852262900569*

[17] Guasto, J. S., Rusconi, R. and Stocker, R. [2012], 'Fluid mechanics of planktonic microorganisms', *Annual Review of Fluid Mechanics* **44**, 373–400.

[18] Halpern, D. and Secomb, T. W. [1992], 'The squeezing of red blood cells through parallel-sided channels with near-minimal widths', *Journal of Fluid Mechanics* **244**, 307–322.

[19] Harada, Y. and Asakura, T. [1996], 'Radiation forces on a dielectric sphere in the rayleigh scattering regime', *Optics Communications* **124**(5,Äì6), 529 – 541.
URL: *http://www.sciencedirect.com/science/article/pii/0030401895007539*

[20] Hecht, E. [2002], *Optics*, Addison-Wesley Longman, Incorporated.
URL: *http://books.google.se/books?id=7aG6QgAACAAJ*

[21] Hinch, E. J. and Leal, L. G. [1979], 'Rotation of small non-axisymmetric particles in a simple shear flow', *Journal of Fluid Mechanics* **92**, 591–607.
URL: *http://journals.cambridge.org/article_S002211207900077X*

[22] Ingber, M. S. and Mondy, L. A. [1994], 'A numerical study of three-dimensional Jeffery orbits in shear flow', *Journal of Rheology* **38**(6), 1829–1843.
URL: *http://link.aip.org/link/?JOR/38/1829/1*

[23] Jeffery, G. B. [1922], 'The Motion of Ellipsoidal Particles Immersed in a Viscous Fluid', *Proceedings of the Royal Society of London. Series A* **102**(715), 161–179.
URL: *http://rspa.royalsocietypublishing.org/content/102/715/161.short*

[24] Johansson, A. [2012], Analysis of empirical data on the tumbling of microrods in a shear flow. M.Sc. Thesis, Chalmers University of Technology.

[25] Leal, G. [2007], *Advanced transport phenomena: fluid mechanics and convective transport processes*, Cambridge; New York: Cambridge Univ. Press.

[26] Leal, L. G. [1975], 'The slow motion of slender rod-like particles in a second-order fluid', *Journal of Fluid Mechanics* **69**, 305–337.

[27] Loth, E. and Dorgan, A. [2009], 'An equation of motion for particles of finite Reynolds number and size', *Environmental Fluid Mechanics* **9**(2), 187–206.
URL: *http://dx.doi.org/10.1007/s10652-009-9123-x*

[28] Mason, S. G. and Manley, R. S. J. [1956], 'Particle Motions in Sheared Suspensions: Orientations and Interactions of Rigid Rods', *Proceedings of the Royal Society of London. Series A. Mathematical and Physical Sciences* **238**(1212), 117–131.
URL: *http://rspa.royalsocietypublishing.org/content/238/1212/117.abstract*

[29] Mehra, R. [2003], 'Application of refractive index mixing rules in binary systems of hexadecane and heptadecane with n-alkanols at different temperatures', *Proceedings Indian Academy of Sciences* **115**(2), 147–154.
URL: *http://www.ias.ac.in/chemsci/Pdf-Apr2003/Pc3260.pdf*

[30] Mishra, Y. N., Einarsson, J., John, O. A., Andersson, P., Mehlig, B. and Hanstorp, D. [2012], 'A microfluidic device for studies of the orientational dynamics of microrods'.
URL: *http://dx.doi.org/10.1117/12.915871*

[31] Neves, A. A. R., Camposeo, A., Pagliara, S., Saija, R., Borghese, F., Denti, P., Iatì, M. A., Cingolani, R., Maragò, O. M. and Pisignano, D. [2010], 'Rotational dynamics of optically trapped nanofibers', *Opt. Express* **18**(2), 822–830.
URL: *http://www.opticsexpress.org/abstract.cfm?URI=oe-18-2-822*

[32] Pierre, F. and Boyer, F. [2013], *Mathematical tools for the study of the incompressible Navier-Stokes equations and related models*, New York, London : Springer.

[33] Romero, C., Agarwala, J. and Davis, R. [1993], 'Separation and classification of axisymmetric particles in an inclined settler', *International Journal of Multiphase Flow* **19**(5), 803 – 816.

[34] Secomb, T. W., Hsu, R. and Pries, A. R. [2001], 'Motion of red blood cells in a capillary with an endothelial surface layer: effect of flow velocity', *American Journal of Physiology - Heart and Circulatory Physiology* **281**(2), H629–H636.

[35] Shearer, S. and Hudson, J. [n.d.], 'Fluid Mechanics: Stokes´ law and viscosity'.
URL: *http://www.engr.uky.edu/ egr101/ml/ML3.pdf*

[36] Sun, X., Li, X. and Zhang, J. [2008], 'Orientating manipulation of cylindrical particles with optical tweezers', *Journal of Nonlinear Optical Physics and Materials* **17**(4), 387–394.

[37] Tlusty, T., Meller, A. and Bar-Ziv, R. [1998], 'Optical gradient forces of strongly localized fields', *Physics Review Letters* **81**(8), 1738–1741.

[38] Trevelyan, B. and Mason, S. [1951], 'Particle motions in sheared suspensions. I. Rotations', *Journal of Colloid Science* **6**(4), 354 – 367.
URL: *http://www.sciencedirect.com/science/article/pii/0095852251900050*

[39] Tucker, W. [2002], 'Computing accurate poincaré maps', *Physica D Nonlinear Phenomena* **171**, 127–137.

[40] Watson, J. [2014], 'Viscosities'.
URL: *http://www.kayelaby.npl.co.uk/general_physics/2_2/2_2_3.html*

[41] Yarin, A. L., Gottlieb, O. and Roisman, I. V. [1997], 'Chaotic rotation of triaxial ellipsoids in simple shear flow', *Journal of Fluid Mechanics* **340**, 83–100.
URL: *http://journals.cambridge.org/article_S0022112097005260*

A

Change of variable in Jeffery's equations

The integrating variable in equations (4.11a) and (4.11c) is changed from t to ϕ by

$$\frac{d\theta}{d\phi} = \frac{d\theta}{dt}\frac{dt}{d\phi} = \frac{d\theta}{dt}\Big/\frac{d\phi}{dt} = \frac{(g_2 \sin\psi + g_3 \cos\psi)\sin\theta}{\frac{1}{2} + g_3 \sin\psi - g_2 \cos\psi}, \tag{A.1a}$$

$$\frac{d\psi}{d\phi} = \frac{d\psi}{dt}\frac{dt}{d\phi} = \frac{d\psi}{dt}\Big/\frac{d\phi}{dt} = \frac{g_1 + (g_2 \cos\psi - g_3 \sin\psi)\cos\theta}{\frac{1}{2} + g_3 \sin\psi - g_2 \cos\psi}. \tag{A.1b}$$

The function $d\phi/dt$ is a monotone function [21], it is therefore invertible, which makes this substitution is allowed. The advantage of doing the substitution is that the time dependency is eliminated, which reduces the dimensionality of the system.